

Modular and Reconfigurable Wireless E-Tattoos for Personalized Sensing

Hyoyoung Jeong, Liu Wang, Taewoo Ha, Ruchika Mitbander, Xiangxing Yang, Zhaohe Dai, Shutao Qiao, Linxiao Shen, Nan Sun, and Nanshu Lu*

In the past few years, ultrathin and ultrasoft epidermal electronics (a.k.a. e-tattoos) emerged as the next-generation wearables for telemedicine, mobile health, performance tracking, human-machine interface (HMI), and so on. However, it is not possible to build an all-purpose e-tattoo that can accommodate such a wide range of applications. Thus, the design, fabrication, and validation of modular and reconfigurable wireless e-tattoos for personalized sensing are reported. Such e-tattoos feature a multilayer stack of stretchable layers of distinct functionalities—a near field communication (NFC) layer capable of wireless power harvesting and data transmission, a functional circuit layer, and a passive electrode/sensor layer. These layers can be disassembled and swapped out multiple times to form different e-tattoos of different sensing capabilities. Such modular and wireless e-tattoos can be rapid-prototyped via a dry, digital, and cost-effective fabrication process—the “cut-solder-paste” process. They have been successfully applied to wirelessly measure a variety of biometrics.

telemedicine, mobile health, prosthetics, athletic training, human-machine interface (HMI) and so on. From “skin-like” electronics (a.k.a. e-skins)^[1] to “epidermal electronics” (a.k.a. e-tattoos),^[2] people are hopeful that the emerging flexible/stretchable electronics technologies will disrupt the wearable industry. Specifically, e-tattoos are ultrathin, ultrasoft membranes that can well conform to the skin to monitor a variety of biomarkers including electrophysiology,^[3] mechano-acoustic signals,^[4] skin temperature,^[5] skin hydration,^[6] skin stiffness,^[7] blood pressure,^[8] blood oxygen saturation,^[9] and even sweat analytes.^[10] Wireless communication enabled by near field communication (NFC)^[9a,11] and Bluetooth^[12] have also been demonstrated in a few recent e-tattoos.

1. Introduction

Wearable electronics capable of high-fidelity, ambulatory physiological monitoring are finding increasing applications in

However, which biomarker to measure is highly personal and may vary from time to time for the same individual. Moreover, different biomarkers should be measured at different locations using different types of sensors and read-out circuits. Even if one can build a multimodal e-tattoo, excessive recordings not personalized to the user may cause unnecessary power and bandwidth consumption, which is a major concern for wireless wearables. Although it is possible to build specific e-tattoos for specific sensing tasks, it would be a big waste of the wireless transmission and read-out circuits if the whole e-tattoo has to be disposed after just one use.


Herein, we propose a possible remedy for all the aforementioned challenges—the modular and reconfigurable e-tattoos, where layers of distinct functionalities (e.g., NFC layer, analog front end (AFE) layer, electrode layer, etc.) can be pre-fabricated as building blocks that can be picked and assembled into customized e-tattoos and can also be swapped out to form new e-tattoos. Electrical connections between the layers can be achieved through aligned vias. Compared with existing monolayer, fully pre-defined e-tattoos, the newly proposed modular and reconfigurable e-tattoos would have the following appealing advantages. First, the multilayer stack can effectively shrink the footprint of the e-tattoo on the skin, especially when numerous components and complex circuits are needed for signal read-out and wireless transmission. Second, when the measurement is done, only the passive electrode/sensor layer that has been in direct contact with the skin needs to be peeled off from the e-tattoo and disposed. As a result, the leftover NFC

H. Jeong, Dr. T. Ha, X. Yang, L. Shen, Prof. N. Sun
Department of Electrical and Computer Engineering
University of Texas at Austin
Austin, TX 78712, USA

L. Wang, Z. Dai, Dr. S. Qiao
Department of Aerospace Engineering and Engineering Mechanics
Center for Mechanics of Solids
Structures and Materials
University of Texas at Austin
Austin, TX 78712, USA

R. Mitbander
Department of Biomedical Engineering
University of Texas at Austin
Austin, TX 78712, USA

Prof. N. Lu
Department of Aerospace Engineering and Engineering Mechanics
Department of Biomedical Engineering
Center for Mechanics of Solids
Structures and Materials
Texas Materials Institute
University of Texas at Austin
Austin, TX 78712, USA
E-mail: nanshulu@utexas.edu

 The ORCID identification number(s) for the author(s) of this article can be found under <https://doi.org/10.1002/admt.201900117>.

DOI: 10.1002/admt.201900117

and functional circuit layers can be reassembled with other electrode/sensor layers to form new e-tattoos. Finally, each layer can be individually altered without affecting the other layers, which offers significant flexibility in e-tattoo modification and upgrading.

In fact, multilayer stretchable electronics have been realized through conductive layer deposition^[9a,11a,b] or laser ablation soldering^[12d], which permit an increased density of electronics and complexity in functionality. However, multilayer stretchable electronics fabricated in those ways are permanently configured, such that they cannot be disassembled into layers without causing any mechanical damage. As a result, we propose a novel “cut-solder-paste” fabrication method for the rapid prototyping of the modular and reconfigurable e-tattoos. It overcomes the difficulty of soldering on polymer substrates as well as disassembly between layers. Furthermore, it is a dry and digital manufacturing approach that is highly labor- and

cost-effective. As a demonstration, we applied this platform for wireless, personalized monitoring of electrocardiogram (ECG), blood oxygen saturation level (SpO₂), and heart rate (HR), as well as skin temperature and skin hydration.

2. Results and Discussion

2.1. Modular and Reconfigurable Design of the Wireless Stretchable e-Tattoos

Schematics and photos of the modular and reconfigurable NFC-enabled e-tattoo are displayed in **Figure 1**. The e-tattoo consists of multiple layers of different functionalities: a generic NFC layer for wireless power and data transmission, a replaceable functional circuit layer for signal read-out that may include AFE and/or amplifier ICs, and an optional disposable gold (Au)

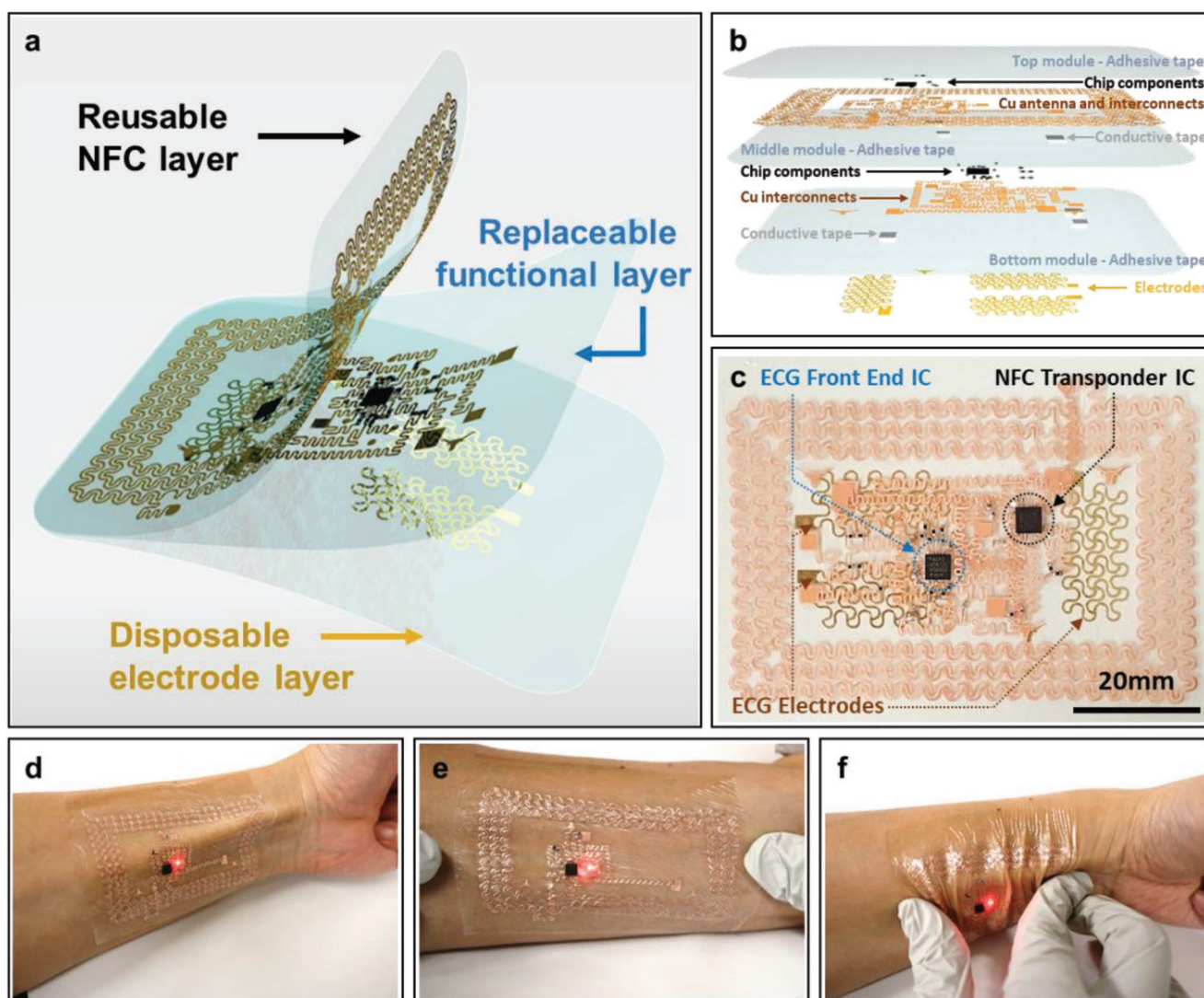


Figure 1. Schematics and photos of NFC-enabled, modularized, stretchable e-tattoo capable of wireless power and data transmission. a) Schematic of the modularized e-tattoo, from top to bottom: NFC module, ECG circuit module, and electrode module. b) Exploded schematic for the same e-tattoo with major components labeled. c) A photo of the assembled ECG e-tattoo. Photos of a wireless e-tattoo with LED worn on the skin powered by a wireless NFC reader concealed beneath the white paper: d) undeformed; e) stretched; f) compressed.

electrode layer for ECG or hydration sensing (Figure 1a). Each layer is supported by a stretchable and transparent 3M Tegaderm tape (thickness 47 μm , modulus 7 MPa measured in our previous work^[13]), which also serves as the dielectric layer between the circuits on different layers. The different layers are pre-defined building blocks that can be selected and assembled through lamination to form a fully functional wireless e-tattoo. Upon finishing the measurements, the Tegaderm adhesive enables the layers to be peeled off from each other and return as building blocks ready for future assembly except the electrode layer. The electrode layer is the only layer that makes direct contact with the skin. As the adhesion degrades due to collected skin exfoliates and also for hygienic reason, the electrode layer should be disposed after one-time use.

Figure 1b offers a schematic of the exploded-view of different components involved in the system. The top NFC layer incorporates a stretchable inductive coupling antenna with double-stranded serpentine design,^[13] stretchable copper (Cu) interconnects, passive and active discrete components such as a thermistor (NTCG104LH104, TDK) and an NFC transponder IC (RF430FRL152H, Texas Instruments). Depending on the application, the next layer can be selected among three different functional circuits for ECG, skin hydration, or SpO_2 . The functional layer for ECG needs to include a commercially available AFE IC for ECG (AD8232, Analog Devices) and corresponding peripheral components. The functional layer for skin hydration incorporates an operational amplifier (LMP2231, Texas Instruments). The functional layer for SpO_2 is comprised of a red light emitting diode (LED) (APTD1608SEC, Kingbright), an infrared LED (SFH 4441, Osram Opto Semiconductors), two photodetectors (TEMT6200FX01, Vishay), and corresponding peripheral components. To carry out ECG or skin hydration sensing, a third layer that just encompasses three separate Au electrodes is necessary. Electrical connections between layers are realized through via holes created in the middle and bottom Tegaderm tapes. A double-sided z-axis conductive tape (ECATT 9703, 3M) is cut to share the same footprint as the via holes, and are applied at each via to adhere aligned Cu contact pads. The tape matrix is filled with conductive microbeads which allow for electrical conduction while providing sufficient adhesion to maintain conductivity while undergoing deformation. Figure 1c is the picture of an assembled e-tattoo with NFC + ECG AFE + electrode layers. A representative block diagram for the modularized e-tattoos is provided in Figure S1 (Supporting Information). Such e-tattoo can be wirelessly powered and read by external interrogators such as USB NFC transponders or an NFC-enabled smart-phones.

In Figure 1d–f, an NFC-enabled wireless e-tattoo of size 7.4 cm \times 5 cm \times \approx 100 μm is laminated and deformed on the human arm. The maximum thickness of the e-tattoo is 1.2 mm where the NFC IC resides. It is important to note that to wear such e-tattoo, the NFC layer with Cu antenna and the functional layer with Cu interconnects should never directly touch the skin for three reasons. First, Cu is not biocompatible. Second, the electrical conductivity of skin can significantly affect the electrical behaviors of the two layers. Lastly, any layer directly contacting the skin is no longer reusable. Therefore, even when we just need the NFC layer for skin temperature measurement or just the NFC layer plus the functional layer for SpO_2 measurement, we should always include a bare Tegaderm layer

between the e-tattoo and the skin. But for ECG & skin hydration e-tattoo, the third layer is the gold electrode layer, which should always contact the skin without any insulating layer. In Figure 1d–f, attached on skin is a clean insulating Tegaderm layer covered by a slightly modified NFC layer which includes one LED for demonstration. The LED on the e-tattoo can be wirelessly turned on by an NFC transponder (TRF7970 EVM, Texas Instruments) hidden under the white paper, even under severe skin deformation. Movie S1 (Supporting Information) demonstrates that even when the arm was lifted by 7 cm, the LED stayed on, indicating the power transfer range up to 7 cm.

2.2. “Cut-Solder-Paste” Method for Manufacturing Modular and Reconfigurable e-Tattoos

The modular e-tattoo is manufactured by a rapid, freeform “cut-solder-paste” method as illustrated in Figure 2. It is upgraded from the “cut-and-paste” process we invented for the rapid prototyping of passive e-tattoos in 2015^[13] to incorporate ICs and enable multilayer architecture. Compared with conventional photolithography plus transfer-printing fabrication of e-tattoos,^[2a,9a,b] the “cut-and-paste” method is a dry and digital fabrication process that can be completed on any desktop within minutes. However, it is not possible to directly solder IC on polymer substrates like Tegaderm. Therefore, we had to come up with a solderable but temporary substrate for IC soldering before pasting the completed circuit on Tegaderm.

To fabricate the NFC layer, an 18 μm thick Cu foil (Copper 110 Annealed, ThyssenKrupp Materials) was laminated on a thermal release tape (TRT) (Heat Release 3196, Semiconductor Equipment Corp) (Figure 2a). The TRT was adhered to a cutting mat and the designed antenna and interconnects were carved into the Cu foil using a mechanical cutter plotter (Silhouette Cameo, Silhouette America) (Figure 2b). Excess Cu was manually peeled off with tweezers (Figure 2c). The leftover Cu antenna and interconnects were then flipped to adhere to a water soluble tape (WST) (water-soluble wave solder tape 5414, 3M) laminated on a Kapton tape (DuPont) backed by a glass slide. To remove the TRT, the glass slide was heated on a hot plate at 120 $^\circ\text{C}$ for about 30 s. After cooling down to room temperature, the TRT was peeled off, leaving the patterned Cu on the WST (Figure 2d). Due to the reasonably high thermal budget of the WST (240 $^\circ\text{C}$) and the Kapton tape (350 $^\circ\text{C}$), electrical components (NFC IC, AFE IC, photodetectors, LEDs, amplifiers, resistors, and capacitors) and interconnecting bridges could be reliably soldered on the Cu circuit using conventional solder paste (Low Temp 138C, Chip Quik) according to the circuit designs (Figure S2, Supporting Information). The glass slide was kept on a hot plate at 220 $^\circ\text{C}$ for 2 min for reflow purpose (Figure 2e). The WST maintained its adhesion and flatness during the soldering process with the support of the Kapton tape. After completing soldering, the circuitry with WST can be pasted on a Tegaderm tape with the Kapton tape being simply peeled off (Figure 2f). The WST was then dissolved by adding water droplets (Figure 2g), leaving behind only IC-incorporated circuitry on Tegaderm (Figure 2h). The generic NFC layer and the functional layers (Figure S2a,c,e, Supporting Information) require two separate “cut-solder-paste”

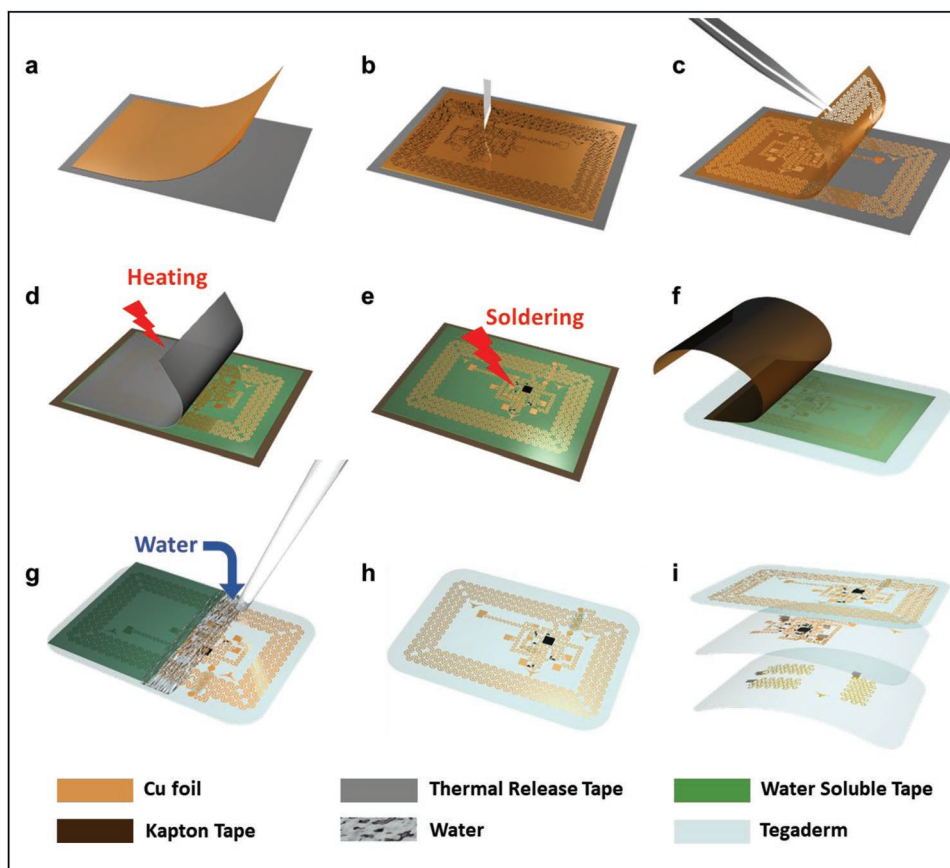


Figure 2. Schematics of the “cut-solder-paste” fabrication process for the modularized e-tattoo. a) Laminating a copper foil on a thermal release tape (TRT). b) A digital mechanical cutter platter carving the copper foil according to imported AutoCAD design. c) Peeling off all of the excess Cu with a tweezer, leaving desirable Cu pattern on the TRT. d) Flipping and transferring the patterned Cu onto a water soluble tape (WST) supported by a Kapton tape mounted on a glass slide by heating and removing the TRT. e) Soldering ICs and other discrete components on the Cu. f) Transferring the finished circuit to a Tegaderm tape and peeling off the Kapton tape. g) Applying water droplets to dissolve the WST. h) Completed single layer e-tattoo. i) Stacking multiple tattoo layers with double-sided conductive tapes adhering via pads on different layers.

processes as illustrated by Figure 2a–h to manufacture whereas the electrode layer can be manufactured by conventional “cut-and-paste” method. Before assembly, via holes should be cut in Tegaderm using a fine point blade and then double-sided z-axis conductive tapes were adhered to each via hole. Using the three longhorn patterns as alignment markers, the NFC layer was stacked onto the functional layer and the stacked bilayer can laminate with the electrode layer if needed (Figure 2i). Lamination should be done slowly and carefully to avoid trapping air bubbles between layers. During the lamination, the step height of the ICs (≈ 1 mm) can be fully accommodated by the local stretching of the soft Tegaderm tape covering the ICs, therefore, causing negligible misalignment for the rest of the circuit. For a well-trained individual, it only takes about 90 min to fabricate one fully functional multilayer e-tattoo, which is ideal for the rapid prototyping of wireless e-tattoos.

2.3. Strain Analysis for the Multilayer e-Tattoo

The structural design of the modular e-tattoo should be guided by mechanical analysis for the following three major reasons.

First, the feature size of the “cut-solder-paste” method has a lower limit of $200\ \mu\text{m}$ dictated by the Silhouette cutter platter, such that we had to play with other parameters such as serpentine arm length to achieve suitable stretchability of the serpentine-shaped interconnects. Second, the multilayer structure can compromise the stretchability of the serpentine ribbons compared with single layer case. Lastly, edges of the rigid components may be susceptible to mechanical failure due to large mismatch of stiffness. According to established serpentine mechanics, narrower, bigger-arc, and longer-armed serpentes are more stretchable.^[14] Considering the limited real estate on each layer, the most feasible way to increase serpentine stretchability was to enlarge the arm length. Rigid electronic components should be distributed as sparsely as possible so that serpentine interconnects in between do not have to carry excessive strain.^[15]

We analyzed the mechanical deformation and strain distribution in the multilayer e-tattoo using commercial finite element modeling (FEM) software ABAQUS/standard 6.13. After iterative design-FEM-redesign procedure, acceptable layouts for each layer are shown (Figure S2, Supporting Information). The modification of each layer is fully decoupled from one another as long as the vias stay aligned thanks to the modular construction. The

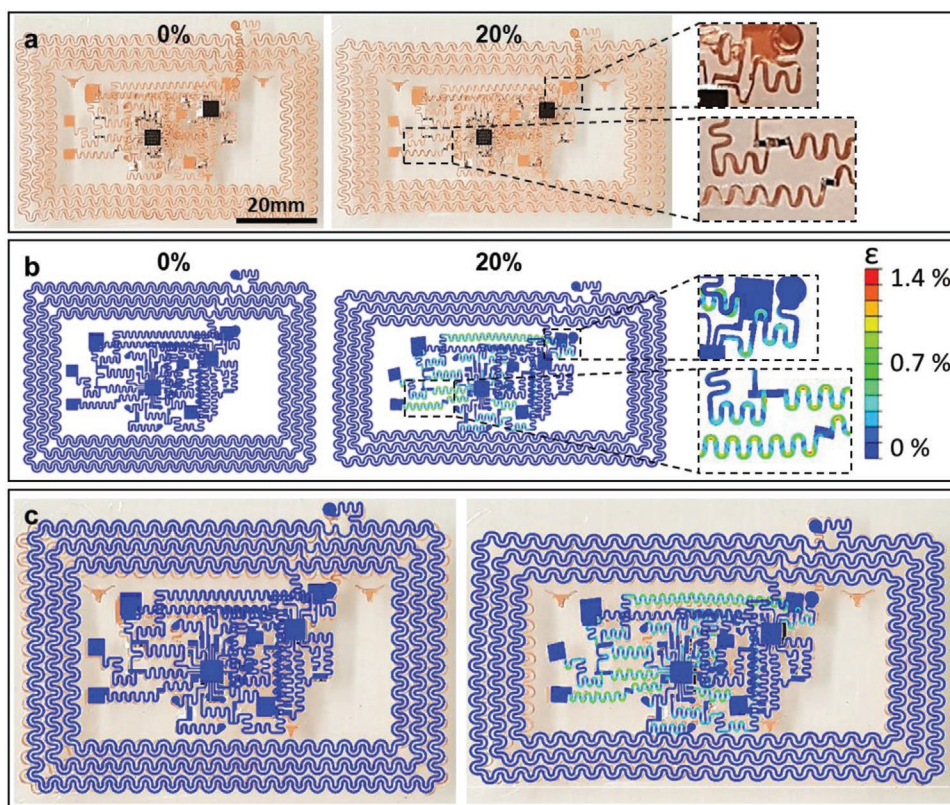


Figure 3. Comparison of the experimental and FEM results of a multilayer e-tattoo under 0 and 20% uniaxial strain. a) Experimental photos of an undeformed and 20% stretched e-tattoo. The insets highlight the most deformed regions of the circuit. b) Corresponding FEM contour plots of the maximum principle strains. c) Experimental and FEM images fully overlapped for undeformed and deformed e-tattoo.

experimental and FEM results before and after 20% uniaxial applied strain are displayed in **Figure 3** for multilayer and single layer e-tattoos (Figure S4, Supporting Information), respectively. As shown in Figure 3a, the double-stranded serpentine antenna (ribbon width of 400 μm , arc radius of 400–1200 μm , arm length of 400 μm) and single-stranded interconnects (ribbon width of 250–400 μm , arc radius of 400 μm , arm length of 800–1200 μm) were designed such that the multilayer e-tattoo can survive skin-tolerable deformation (20%) without any mechanical or electrical failure. Corresponding FEM results are provided in Figure 3b, where regions with maximum strains are blown up. The FEM results suggest that when stretched by 20%, the maximum strain in the serpentine of the carefully designed multilayer e-tattoo is bounded by 1.4%, which occurs at the inner crests of the serpentine ribbons, instead of the roots of the rigid components, which corresponds well with the experimentally observed serpentine rupture sites (Figure S3c, Supporting Information). We also found that the maximum strain in serpentine only increases from 0.6% in single layer (Figure S4b, Supporting Information) to 1.4% after adding more layers (Figure 3b). It is because the Young's modulus of Tegaderm (7 MPa) is four orders lower than that of Cu (130 GPa^[16]). The fully overlapped experimental and FEM results in Figure 3c and Figure S4c (Supporting Information) validate our FEM analysis. We also confirmed experimentally that the e-tattoo was able to operate wirelessly without mechanical and electrical failure under different kinds of deformation such as stretching (Movie S2,

Supporting Information), bending (Movie S3, Supporting Information), and folding (Movie S4, Supporting Information).

2.4. Electromagnetic Characteristics of the e-Tattoo under Deformation

Beyond pure mechanical considerations, we also need to examine the electromagnetic-mechanical coupling of the planar stretchable antenna (PSA) on our e-tattoo because the characteristics of the PSA is crucial for wireless data and power transmission. The basic requirements for PSA can be summarized as: i) it should have proper dimensions and number of turns for suitable inductance,^[13] ii) it should be stretchable, and iii) its resonance frequency should be relatively insensitive to mechanical deformation. **Figure 4** and Figures S5 and S6 (Supporting Information) describe the experimental and FEM studies on the electromagnetic-mechanical behaviors of the PSA. To measure the resonance frequency (f_{res}) of the PSA, a 10 cm diameter single loop reader coil formed by a 22 gauge Cu wire was connected to a Vector Network Analyzer (VNA) (N5225A, Agilent Technologies) and then inductively coupled to the PSA as shown in Figure 4a,b. PSA in three different devices as illustrated in Figure 4c were measured on skin and in air under tension and bending. The corresponding S11 plots are provided in Figure S5b–f (Supporting Information).

Plotting f_{res} as a function of applied uniaxial tensile strain on a freestanding PSA in Figure 4d suggests that the f_{res} only decreased

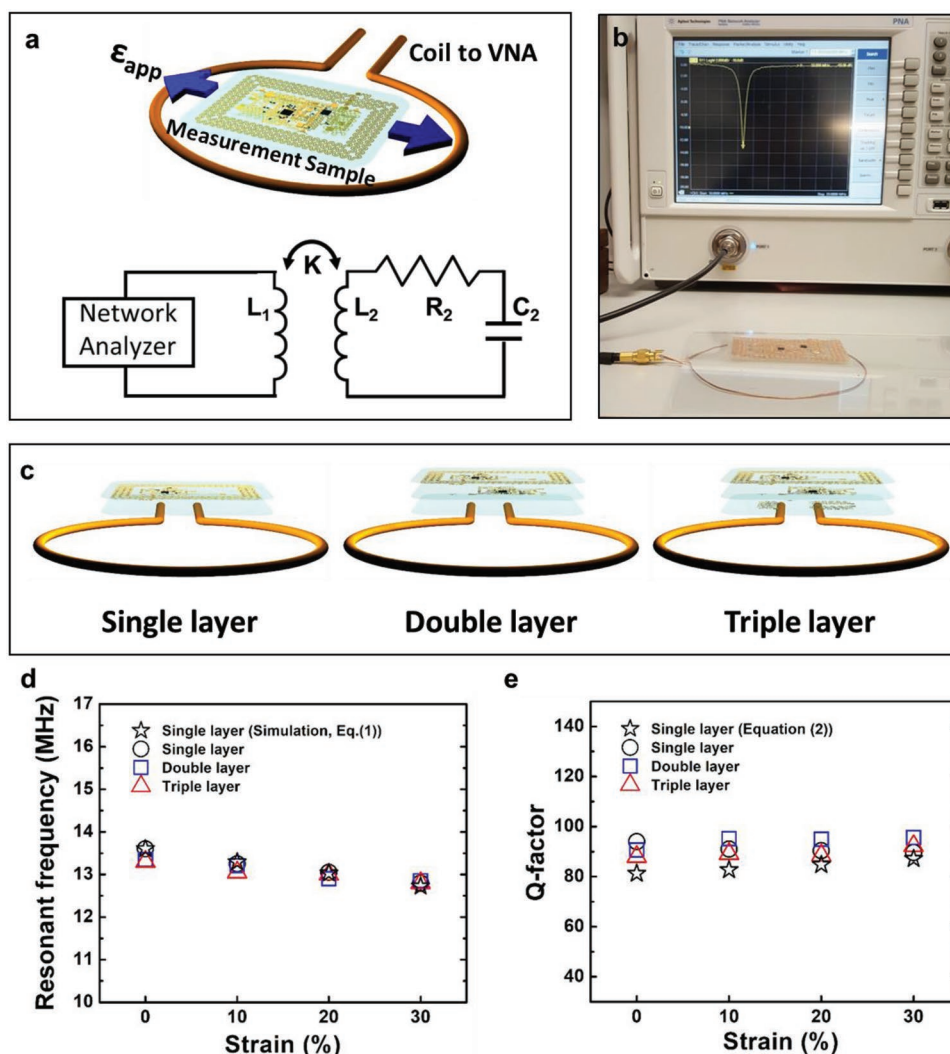


Figure 4. Electromagnetic-mechanical characteristics of e-tattoos. a) A schematic of the resonance frequency (RF) measurement setup. Inset is the simplified circuit diagram for the setup. b) A photo of the experimental setup. c) Schematics for single, double, and triple layer e-tattoos during RF measurement. d) Measured and calculated RF under 0, 10%, 20%, and 30% of applied uniaxial tensile strain of the e-tattoos. e) Measured and calculated Q-factor under 0, 10%, 20%, and 30% of applied uniaxial tensile strain of the e-tattoos.

by 5.8% (13.6 to 12.8 MHz) after stretched by 30%. Hybrid mechanical and electromagnetic FEM was also applied to characterize the electromagnetic-mechanical coupling in PSA. The mechanical deformation of single-layer PSA was modeled using ABAQUS structural analysis and the deformed shapes (Figure S6, Supporting Information) were then imported into ANSYS Maxwell for inductance calculation. L_2 was simulated to be 4.49, 4.7, 4.89, and 5.13 μH under strains of 0%, 10%, 20%, and 30%. More details about the simulation procedure can be found in the Experimental Section. According to measured f_{res} and FEM simulated L_2 at 0%, we can obtain $C_2 = 30$ pF according to Equation (1) in the Experimental Section. Assuming $C_2 = 30$ pF is unchanged during stretch and plugging the simulated L_2 at different strains into Equation (1), we can plot the calculated f_{res} as stars in Figure 4d. The good agreement between the measured and calculated f_{res} validates our hybrid mechanical and electromagnetic FEM. Q-factor defined in Equation (2) in the Experimental Section as a function of strain is plotted in Figure 4e. The Q-factor of undeformed

single layer e-tattoo (circles in Figure 4e) was measured to be 94 but dropped slightly to 89 under 30% strain. The measured Q-factor for single, double and triple layer e-tattoos vary slightly with applied strain. Note that the calculated Q-factor according to Equation (2) (stars in Figure 4e) increases slightly with the strain as L_2 enlarges with tensile strain. But the change of capacitance with strain was not considered in the calculation, which could be responsible for some of the discrepancies between the measured and calculated Q-factors.

2.5. Four Sensing Modalities of the Personalized e-Tattoos

With proper design and comprehensive characterization, we were able to demonstrate four sensing modalities of our battery-free, wireless e-tattoos: ECG, SpO₂ and HR, skin temperature, and skin hydration in single- or dual-mode operation according to the personal needs of different users.

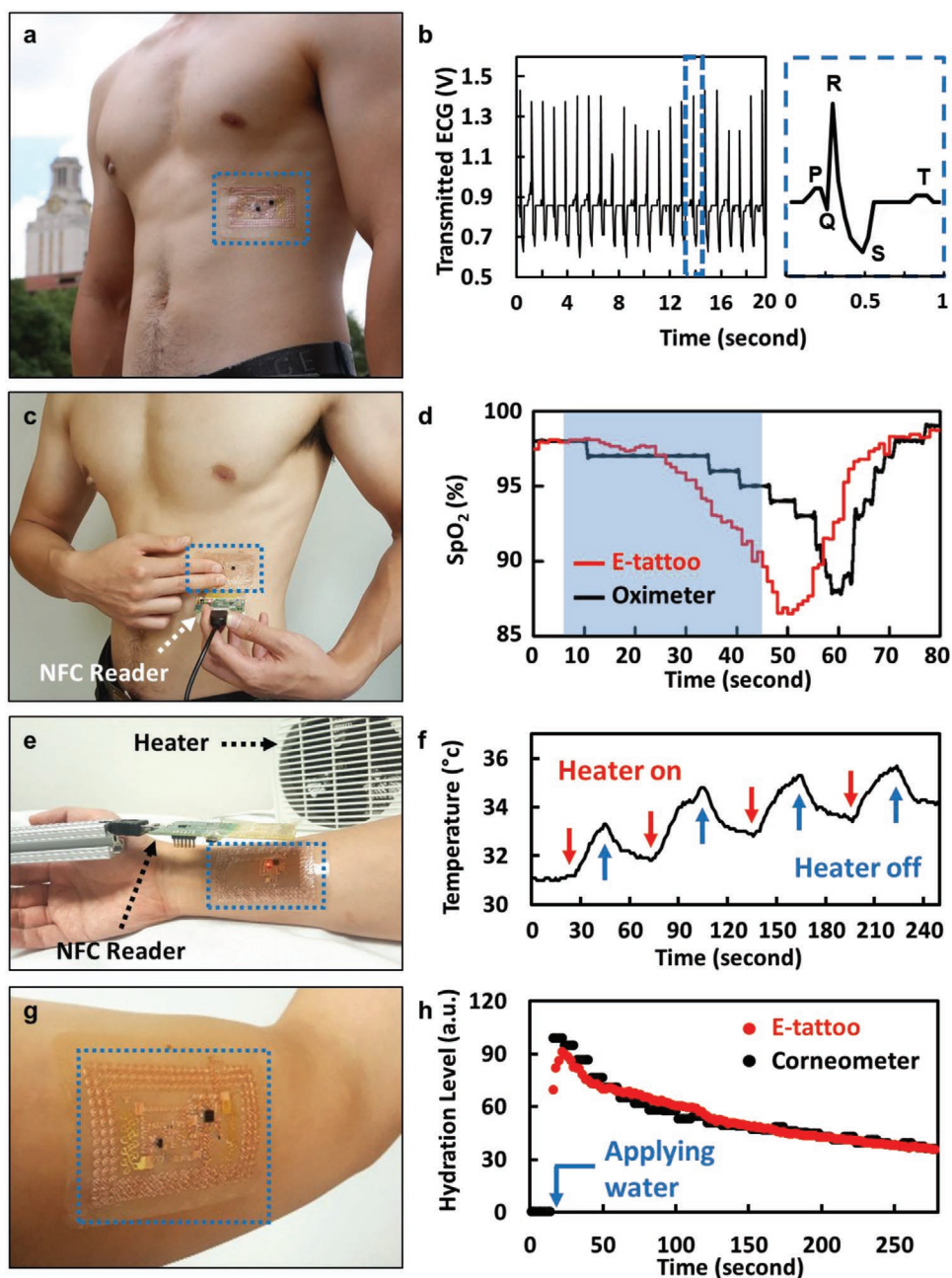


Figure 5. Four sensing modalities of the NFC-enabled e-tattoos. a) A picture of the battery-free ECG e-tattoo applied at the lower rib cage of a male subject. b) Wirelessly measured ECG by the e-tattoo. Magnified view of the ECG signal in the blue dashed box clearly shows the PQRST wave. c) A picture of the SpO₂ e-tattoo on skin with two fingers covering the red and IR LEDs. d) SpO₂ measured wirelessly by the e-tattoo (red) and by a commercial oximeter (black) before, during (blue shade), and after apnea. e) A picture of a temperature sensing e-tattoo on human wrist with heater blowing intermittently. f) Wirelessly measured skin temperature from the e-tattoo. Red and blue arrows indicate the moments of turning on and off the heater, respectively. g) A picture of the hydration sensing e-tattoo on the upper arm. h) Wirelessly measured skin hydration by the e-tattoo (red) and a commercial corneometer (black) before and after water application on the skin.

2.5.1. NFC-Enabled ECG Sensing e-Tattoo

Although battery-free ECG sensing e-tattoos based on radio frequency (RF) transmission have been demonstrated,^[12b,17] it required bulky interrogators. As a result, here we demonstrate ECG sensing using NFC e-tattoo. We placed the ECG e-tattoo at the lower rib cage of a human subject as shown

in Figure 5a. This location was chosen for the wider R peak in the ECG compared with ECG measured from human chest.^[12c] The recorded raw ECG was first saved in the non-volatile memory of the NFC IC and then transmitted to a laptop through a USB NFC transponder. The reader coil was able to read the ECG when placed parallel with the e-tattoo as far as 7 cm away. Figure 5b displays the ECG data measured from

the lower rib cage at 25 Hz sampling rate, which has distinguishable QRST waves in the blown-up view. The waveform is similar to the ECG measured by a flexible printed circuit board based ECG sensor at the lower rib cage in a previous study.^[12c] Unfortunately, 25 Hz sampling rate is the upper limit of all current NFC ICs on the market although it is not a fundamental limit of NFC. The signal quality of the ECG measured by NFC e-tattoo would be sufficient for heart rate extraction^[11c] but not waveform analysis.

2.5.2. NFC-Enabled SpO₂ Sensing e-Tattoo

The ECG e-tattoo can be easily reconfigured to read SpO₂. We started by peeling off the electrode layer and the ECG circuit layer altogether to free the generic NFC layer. We then attached a SpO₂ functional layer to this NFC layer to easily reconfigure to a SpO₂ e-tattoo. The SpO₂ functional layer includes red and IR LEDs and their respective photodiodes. The individual layers and the integrated SpO₂ e-tattoo are displayed in Figure S2e,f (Supporting Information). Figure 5c shows the SpO₂ e-tattoo mounted on a subject's lower rib cage with the LEDs and photodetectors facing out. As soon as fingers cover the LEDs on the e-tattoo, two-channel reflected light intensity output from the two photodetectors can be read wirelessly by the USB-powered NFC reader. Two photoplethysmogram (PPG) measured by the two LEDs and the conversion from PPG to SpO₂ are discussed in the Experimental Section. The end result of the SpO₂ is plotted in Figure 5d, where the apnea period is blue-shaded. The red curve was obtained from our SpO₂ e-tattoo and the black curve was recorded by a commercial oximeter (SOMNotouch NIBP, SOMNOMedics GmbH). A drop in SpO₂ level, from 98% to 87%, was detected by the e-tattoo after 40 s of apnea. A similar decrease, from 98% to 88%, was confirmed by the commercial device. However, SpO₂ measured by the commercial oximeter exhibit a delay of 10 s compared with the e-tattoo result. This could be attributed to the larger built-in moving average window in the commercial oximeter (exact size unknown) than that in our e-tattoo (5 s). Similar delay between a customize SpO₂ sticker and commercial oximeter has been observed by other researchers.^[9c] Movie S5 (Supporting Information) demonstrates that an NFC-enabled smart-phone can simultaneously measure the reflective red and IR PPGs from the SpO₂ e-tattoo.

2.5.3. NFC-Enabled Skin Temperature and Skin Hydration Dual-Mode e-Tattoo

NFC-based skin temperature sensors have been achieved before.^[15] To demonstrate our modular e-tattoo is also able to wirelessly sense skin temperature using a thermistor integrated on the NFC layer, the e-tattoo was attached on a subject's wrist with a heater fan blowing to it, as shown in Figure 5e. Figure 5f plots the continuously measured skin temperature when the heater was turned on and off, repeatedly.

Skin hydration can be reflected by either electrical resistance/impedance^[18] or thermal conductivity^[11d,19] of the skin. NFC-enabled battery-free skin hydration e-tattoos are reported

very recently,^[11d] but the overall tattoo is not stretchable and skin hydration is inferred from measured skin thermal conductivity. In contrast, our e-tattoos are fully stretchable and measure electrical resistance of the skin. The e-tattoo can record skin conductance by applying a DC voltage (≈ 0.5 V to noninverting input terminal of noninverting operational amplifier) and measuring the induced current in the skin across the two electrodes in contact with the skin (inverting input terminal of noninverting operational amplifier). The skin conductance to skin hydration relation should be calibrated according to the procedures described in our previous publications.^[13,20] Approximately 5 min of skin conductance data was wirelessly collected from the e-tattoo attached on the upper arm after applying some water to the skin (Figure 5g) and reference data was simultaneously and independently acquired using a commercial corneometer (MoistureMeterSC Compact, Delfin Inc.). The e-tattoo data and reference data are plotted together in Figure 5h, which almost overlap with each other. We can find a sharp increase of hydration right after applying water on the skin, followed by a gradual decrease of hydration in the process of water evaporation.

2.6. Reusable and Waterproof Characteristics of the e-Tattoos

One complete e-tattoo may include reusable, replaceable, and disposable modules. The reusability is demonstrated in **Figure 6**. Each layer represents a module, which is always supported by a transparent Tegaderm tape with adhesive on just one side. Although Tegaderm adhesive is not reusable after peeling off from the skin due to skin exfoliates collected by the adhesive, it can be peeled off (Figure. 6a,b) and relaminated (Figure 6c,d) multiple times to the nonsticky side of other Tegaderm tapes. Moreover, the peeling and lamination processes did not induce any noticeable damage to any of the layers even after 20 iterations of disassembly and assembly of a SpO₂ e-tattoo which consists of the NFC module (with thermistor and reference resistor) and the SpO₂ module. To maintain electrical conductivity between NFC module and SpO₂ module layers, the double-sided z-axis conductive tape was employed disposably, and was replaced every iteration during testing. The wirelessly measured ambient temperature from the initially assembled e-tattoo to the 20th time assembled e-tattoo are plotted in Figure 6e and no degradation in data can be observed. To prove that peeling bilayer is as easy as peeling a single layer, Figure S7 (Supporting Information) shows an e-tattoo consisting of NFC with thermistor, ECG circuit, and electrode layers. Again, consistent ambient temperature can be wirelessly measured after 10 iterations as plotted in Figure S7e (Supporting Information). Thus, we have demonstrated that different modules can be assembled and disassembled multiple times without any mechanical or electrical failure, which enables the reusability of the NFC and circuit modules that do not have to directly contact with the skin.

Another feature to highlight is that the e-tattoos are shower compatible because Tegaderm is allegedly waterproof. Movie S1 (Supporting Information) demonstrates that the wireless e-tattoo remained functional even when water was running over it.

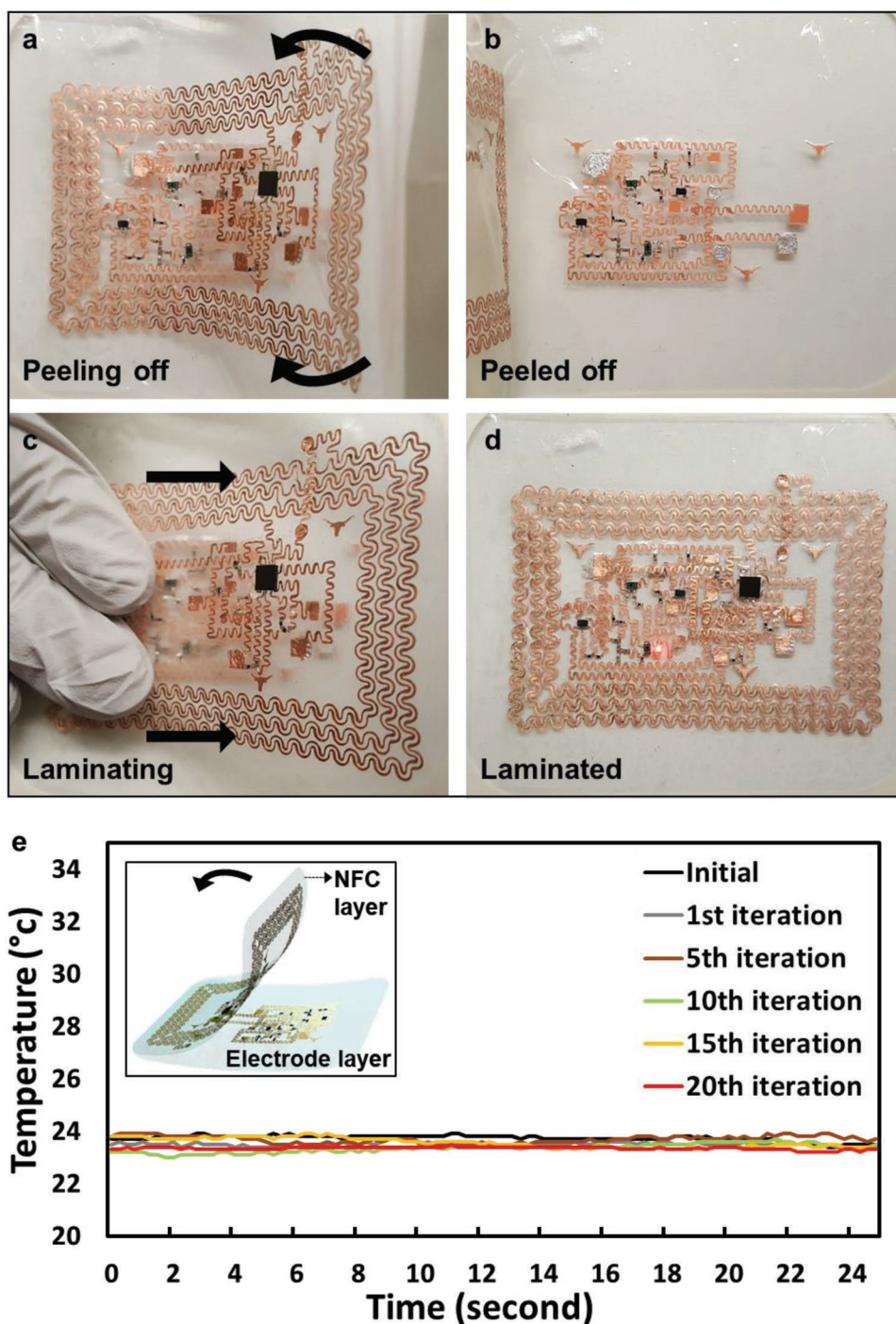


Figure 6. Repeated assembly and disassembly of the SpO_2 e-tattoo. a) Disassembling the SpO_2 e-tattoo by peeling off the NFC layer from the SpO_2 functional layer. b) Image of the disassembled SpO_2 e-tattoo after disassembling and reassembling 20 times. c) Laminating the NFC layer on the SpO_2 e-tattoo after disassembling and reassembling 20 times. d) Image of the assembled SpO_2 e-tattoo after disassembling and reassembling 20 times. e) Wirelessly measured ambient temperature after 1st, 5th, 10th, 15th, and 20th assembly. Inset is a schematic of the SpO_2 e-tattoo.

3. Conclusion

The ultimate success of e-tattoos is tied to their functionality, wearability, and cost. The modular and reconfigurable e-tattoos discussed here have opened the door for highly versatile sensing modalities suitable for personalized use. The reusable

modules help save the cost of passive and active ICs. The “cut-solder-paste” fabrication process reported in this paper is not only useful for the labor- and cost-effective rapid prototyping of e-tattoos, but more broadly for any soft and stretchable circuits which need to incorporate rigid components. Wireless power transmission via NFC offers a remedy to retain the ultrathin

and ultrasoft features of e-tattoos by getting rid of bulky batteries. The conformability, deformability, and water compatibility of the wireless e-tattoos add up to improved wearability. The four sensing modalities demonstrated the capabilities of the wireless e-tattoos but the possibilities are not limited to the four. In addition to vital sign monitoring on human body, modular and wireless soft sensors should also be able to find wide applications for internet of things (IoT).

4. Experimental Section

Electronic Components for e-Tattoos: The major electronic components used in the e-tattoos as labeled in Figure S2 (Supporting Information) are listed as follows: NFC (RF430FRL152H, 4.15 mm × 4.15 mm × 1.00 mm), ECG front end IC (AD8232, 4.00 mm × 4.00 mm × 0.80 mm), amplifier for hydration e-tattoo (LMP2231, 3.00 mm × 3.05 mm × 1.1 mm), amplifier for SpO₂ (MCP6001, 2.20 mm × 2.70 mm × 0.90 mm), red LED (APTD1608SEC/J)3, 1.60 mm × 0.80 mm × 0.95 mm), IR LED (SFH 4441, 2.30 mm × 1.95 mm × 0.90 mm), phototransistor (TEMT6200FX01, 2.00 mm × 1.25 mm × 0.85 mm), and NTC thermistor (NTCG164LH104, 1.60 mm × 0.80 mm × 0.80 mm).

Electromagnetic Coupling under Deformations: Electromagnetic coupling between e-tattoo and the antenna, which is significant in determining the working distance of e-tattoos, was studied by combined analytical and experimental methods. The resonance frequency (f_{res}) of the PSA on the e-tattoo was measured using the setup shown in Figure 4a when subjected to applied tensile strains up to 30%. The reader coil (10 cm diameter) should be larger than the size of the e-tattoo so that the e-tattoo was immersed in the uniform magnetic field generated by the reader coil in a way that the coupling coefficient k was minimally affected by the alignment between the reader coil and the e-tattoo.^[21] The VNA was set in S11 magnitude (reflection) mode to measure the f_{res} and -3dB bandwidth of the PSA (B_{-3dB}). The f_{res} of the PSA can be determined as the location of the minimally reflected power in the magnitude versus frequency spectrum as displayed in Figure S5 (Supporting Information). As illustrated in the equivalent circuit of the PSA shown in Figure 4a, the f_{res} can be expressed as

$$f_{res} = \frac{1}{2\pi\sqrt{L_2C_2}} \quad (1)$$

where L_2 is the effective inductance of the PSA and C_2 is the total capacitance in the e-tattoo which consists of the intrinsic on-chip capacitance of the NFC IC (35 pF with a tolerance of ±10%), coil capacitance, substrate distributed capacitance,^[22] and the external capacitance including the parasitic capacitance generated by the nonideal environment. The quality of the inductive coupling is characterized by the Q-factor, which measures the sharpness of the resonance peak and is defined as f_{res}/B_{-3dB} , where B_{-3dB} represents the -3dB bandwidth of the same spectrum. Analytically, the Q-factor can be calculated by

$$Q = \frac{1}{R_2} \sqrt{\frac{L_2}{C_2}} \quad (2)$$

where R_2 is the total resistance of the PSA, which was measured to be almost constant (4.72 Ω) from 0% to 30% strain.

Bending tests were also carried out to test the electromagnetic-mechanical coupling of the PSA when subjected to out-of-plane deformation as shown in the lower panel of Figure S5a (Supporting Information). The e-tattoo was wrapped around a tube of 1.6 cm diameter, smaller than the size of adult fingers. Figure S5b (Supporting Information) indicates that the f_{res} increased and the resonant peaks lowered and broadened after bending. This is mainly because the magnetic flux through the e-tattoo antenna was reduced after bending. Movies S2–S6 (Supporting Information) demonstrate the flexibility

and stretchability of the e-tattoo. Even after stretched by 20%, or fully wrapped over the 1.6 cm diameter tube, or self-folded, the e-tattoo was still capable of wireless power and data transmission. When measured on skin, the single and double layer e-tattoos were insulated from the skin by a bare Tegaderm tape but for the triple layer e-tattoos, Au electrodes on the electrode layer were in direct contact with the skin. Figure S5c (Supporting Information) confirms the well-known fact that the body loading can decrease the f_{res} of the PSA.^[13,23] Figure S5c (Supporting Information) shows that after putting the e-tattoos on skin, the f_{res} shifted from 13.6 MHz (single layer), 13.35 MHz (double layer), and 13.3 MHz (triple layer) to 11.0, 11.4, and 11.45 MHz, respectively, which was the result of body loading. Body loading also lowered the Q-factors from 94 (single layer), 90 (double layer), 87 (triple layer) to 38, 41, and 45, respectively. The effect of body loading is therefore the least for the triple layer e-tattoo as expected. Despite the body loading effect, all the e-tattoos were able to operate at reasonably high Q-factors when laminated on human skin, even under severe skin deformation, as evidenced in Figure 1d–f and Movie S1 (Supporting Information). In summary, compared with stretching and bending, body loading has induced the most significant change to the f_{res} and Q-factor of the e-tattoo but none of those effects were severe enough to cutoff wireless power and data transmission.

Stretchability Tests with Rigid Components and Varying Serpentine Arm Length: Figure S3 (Supporting Information) investigates the effects of serpentine arm length and rigid component through experiments. Three LEDs were wired to a multichannel digital multimeter (DMM) and a power supply via three different serpentine interconnects. When uniaxially stretched by the same Tegaderm substrate, the explosion of the measured electrical resistance and the extinction of the LED can both give measurements for the strain-to-rupture of the circuit: 16.5% and 14.3% for the short-armed serpentine, 28.5% and 28.6% for the mid-armed serpentine, and 52.5% and 48.6% for the long-armed serpentine (Figure S3b,c, Supporting Information). By examining the location of the rupture (Figure S3c, insets, Supporting Information), it is evident that none of the ruptures occurred right next to the rigid LED. Instead, all mechanical failures were found in the middle of the serpentine ribbons. This observation was also true for circuits containing larger rigid components such as the NFC chip. Such experiments verified that longer-armed serpentine are more stretchable. More importantly, they justified that the solder was strong enough to hold the rigid components to the Cu interconnect under stretching and that the stretchability of the chip-interconnect interface is beyond that of serpentine ribbons.

Mechanical FEM for the Multilayer e-Tattoo: The mechanical strain of the Cu PSA and interconnects in the multilayer e-tattoo have been analyzed by FEM as plotted in Figure 3 and Figure S4 (Supporting Information). FEM was performed via ABAQUS/standard 6.13 to reveal the strain distribution when stretched up to 20%. Because the thickness of the Tegaderm (47 μm) is much smaller than the lateral dimensions of the e-tattoo (7.4 cm × 5 cm), the Tegaderm was modeled as shell elements (S4R). For simplicity, to simulate the Cu-Tegaderm overlapping area, a partition of exactly the same shape as the NFC Cu layout was created on the top face of the Tegaderm. Within the partition, the section thickness was assigned as the total thickness of the Cu and Tegaderm

$$h_{total} = h_{cu} + h_{teg} \quad (3)$$

where h_{cu} , h_{teg} are the thicknesses of Cu and Tegaderm, respectively. The material modulus was assumed as the composite modulus given as

$$E_{eff} = \frac{E_{cu}h_{cu} + E_{teg}h_{teg}}{h_{cu} + h_{teg}} \quad (4)$$

where E_{cu} , E_{teg} are the Young's moduli of Cu and Tegaderm, respectively. Outside the partition, the section thickness and material properties are the same as pure Tegaderm.

Similarly, the Cu interconnect and Tegaderm were also merged into one effective part. Tie constraints were applied between three parts (effective NFC Cu layout, effective circuitry Cu layout, and Tegaderm) in ABAQUS

because they were well adhered by Tegaderm adhesives and no interlayer slippage was observed. The positions of the rigid chip components (modeled as the rigid parts) and the serpentine-shaped interconnects were optimized using FEM to minimize the strain upon stretching.

Electromagnetic FEM for the Multilayer e-Tattoo: To carry out electromagnetic simulation for the PSA, undeformed and deformed PSA were imported to ANSYS Maxwell to simulate the inductance. A 3D model was generated with rectangular cross-section $18 \mu\text{m} \times 400 \mu\text{m}$ assigned to the serpentine ribbon that forms the antenna coil. To simulate the dielectric effect of the surrounding air, the coil was immersed in a rectangular box of atmosphere in the size of $500 \text{ mm} \times 500 \text{ mm} \times 750 \text{ mm}$. Then two wires were extended from the coil to the boundary of the air box, and a current excitation of 1 A was injected to the two output ports. After the simulation, the coil inductance showed up directly in the result output window with magnetic flux density field (B field) distribution of the deformed coils (Figure S6, Supporting Information). Resonance frequencies at different strains in Figure 4d were calculated using Equation (1) with L_2 obtained from the FEM and constant $C_2 = 30 \text{ pF}$. Q-factors at different strains in Figure 4e were calculated using Equation (2) with L_2 obtained from the FEM assuming $C_2 = 30 \text{ pF}$ and $R_2 = 4.72 \Omega$ are constants.

ECG Measurements and Data Analysis: The NFC-enabled ECG sensing e-tattoo consists of the NFC layer, the ECG circuit layer, and the electrode layer. Pictures for the individual layers and the integrated ECG e-tattoo are displayed (Figure S2a,b, Supporting Information). The ECG circuit was designed with two-pole high ($>0.5 \text{ Hz}$) and low ($<40 \text{ Hz}$) pass filters in sequence for reducing motion artifacts. The total gain was 1100, 100 in the instrumentation amplifier and 11 in the second operational amplifier. The electrode layer houses three filamentary-serpentine-shaped stretchable Au electrodes^[13] for common-mode rejection. When mounting the ECG e-tattoo on human lower rib cage, the collected ECG appeared to be the strongest and cleanest compared with signals from other locations.^[12c] It is important to note that the measured ECG is highly sensitive to the location of the ECG e-tattoo because the sampling rate of the NFC IC we used (RF430FRL152H, Texas Instruments) is limited to 25 Hz. If the duration of the R peak in ECG is less than 40 ms (i.e., frequency higher than 25 Hz), the R peak cannot be observed after analog to digital conversion (ADC). The duration of the R peak on chest and lower rib cage were measured using oscilloscope (DS1054Z, Rigol) as shown (Figure S8, Supporting Information). The duration of the R peak was shorter than 40 ms on the chest and 52 ms near the lower rib cage area. Figure S8c (Supporting Information) demonstrates that some of the R peaks could be completely absent when ECG was acquired by the ECG e-tattoo from the chest (red curve). In contrast, all the R peaks clearly present when ECG was measured from the lower rib cage area (black curve).

Pulse Oximetry Measurements and Data Analysis: The SpO_2 e-tattoo was mounted on subject's lower rib cage area and signals were recorded wirelessly by a USB NFC transponder (TRF7970 EVM, Texas Instruments) as shown in Figure 5c. A commercial oximeter was placed on the index finger of the subjects' right hand as a reference device. SpO_2 level was collected for 3 min with normal breathing for 60 s, halted breathing for 40 s, and normal breathing again for 80 s in order to induce changes in SpO_2 . SpO_2 simultaneously measured by the e-tattoo and the oximeter are plotted in Figure 5d. To evaluate the performance of the SpO_2 e-tattoo, a clinically validated oximeter (SOMNOTouch NIBP, SOMNOMedics GmbH) was used as the reference device to measure SpO_2 before, during and after 40 s of apnea. Figure S9a,b (Supporting Information) plot the dynamic PPG (i.e., the reflected light intensity), the Red/IR PPG ratio, and the SpO_2 measured by the reference device and by our SpO_2 tattoo, respectively. The SpO_2 reading from our e-tattoo can be calculated out of the PPG ratio following the process detailed in the literature.^[11b,24] Overall it is obvious that the PPGs measured by the reference device and the e-tattoo are well correlated. The blue-shaded region (from 5 to 45 s) labels the apnea period, during which PPG signals measured by both devices decrease gradually. Figure S9c (Supporting Information) blows-up 15 s signals collected by the e-tattoo, from top to bottom: reflected light intensity output from the photodetectors (red and

IR), band-pass-filtered (0.5–3 Hz) signal, extracted heart rate (HR), and SpO_2 level. The SpO_2 data collection involved a sampling rate of 12.5 Hz for each photodetector which measured reflected light intensity from red (640 nm) and IR (940 nm) LEDs (Figure S9, Supporting Information). Collected data was then analyzed using a commercial program (LabVIEW 2015, National Instruments). Reflected light intensity from two different LEDs can be combined to indicate blood oxygen saturation because oxygenated hemoglobin and deoxygenated hemoglobin absorb 640 and 940 nm wavelengths of light differently.^[25] To extract the AC and DC components, an eighth-order Butterworth band-pass filter of 0.5–3 Hz was designed for $AC(t)$ and an 8th order Butterworth low-pass filter of 0.2 Hz was designed for $DC(t)$. The double-ratio of the AC and DC components of the red and IR absorption, $R(t)$, was calculated every second with a 5 s data acquisition window^[9b,11b]

$$R(t) = \frac{\ln\left(\text{rms}\left(\frac{AC(t)_{\text{RED}}}{DC(t)_{\text{RED}}}\right) + 1\right)}{\ln\left(\text{rms}\left(\frac{AC(t)_{\text{IR}}}{DC(t)_{\text{IR}}}\right) + 1\right)} \quad (5)$$

Finally, oxygen saturation can be computed using the following equation which is derived from photon-diffusion analysis and the differential path length factor (DPF) method based on a modified Lambert-Beer law.^[11b]

$$\text{SpO}_2(t) = \frac{\epsilon_{\text{red,Hb}} \text{DPF} - \epsilon_{\text{IR,Hb}}(R(t))}{(\epsilon_{\text{red,Hb}} - \epsilon_{\text{red,HbO}_2}) \text{DPF} + (\epsilon_{\text{IR,HbO}_2} - \epsilon_{\text{IR,Hb}}) R(t)} \quad (6)$$

where $\epsilon_{\text{red,Hb}}$, $\epsilon_{\text{IR,Hb}}$, $\epsilon_{\text{red,HbO}_2}$, and $\epsilon_{\text{IR,HbO}_2}$ are the molar absorptivity of deoxyhemoglobin at red and infrared wavelengths, the molar absorptivity of oxyhemoglobin at red and infrared wavelengths, and the differential path length parameter, respectively.^[26]

Skin Temperature and Hydration Measurements and Calibration: Skin temperature and skin hydration can be wirelessly measured by one e-tattoo. Compared with ECG and SpO_2 measurements, relatively low sampling rates (e.g., 0.5 Hz) would be sufficient. An NTC thermistor (4550K β constant) can be easily integrated on the NFC layer but skin hydration sensing requires a functional circuit layer and an electrode layer to be sequentially laminated on the NFC layer. Photos for the individual layers and the integrated e-tattoo are displayed (Figure S2c,d, Supporting Information). To verify the temperature sensing capability of the e-tattoo, the NFC layer with the thermistor was placed on a hot plate alongside a reference device (TMD-56 thermocouple, Amprobe). Temperature measured by the e-tattoo was collected wirelessly by a commercial USB NFC reader coil. Figure S10a (Supporting Information) plots the temperature measured by the e-tattoo as a function of the temperature measured by the thermocouple when the e-tattoo was undeformed (black), stretched by 10% (blue), and 20% (red). Strong correlation ($R^2 > 0.99$) can be maintained even when the e-tattoo was stretched. Time-stability of the e-tattoo thermistor under different strains is validated (Figure S10b, Supporting Information). Since we used the same e-tattoo for three different cycles represented by solid, dashed, and dotted curves, there was slight mismatch in hotplate temperature from cycle to cycle. But it is evident that for each cycle, the temperature measured by the e-tattoo matched with the thermocouple and stayed stable until the hotplate temperature was changed to the next level.

Skin hydration measurement were carried out on a healthy male. To hydrate the skin at his upper arm, the skin was rubbed with wet tissue and then laminated by a skin hydration e-tattoo with a through hole engineered between the electrodes. As soon as the e-tattoo was coupled with the USB NFC transponder, the hydration data (0.5 Hz sampling rate) was saved in the nonvolatile memory of the NFC IC. Reference data was simultaneously and independently recorded through the pre-engineered hole on the e-tattoo using a commercial corneometer (MoistureMeterSC Compact, Delfin Inc.). Transmitted e-tattoo raw data $E_{\text{tcal}}(t)$ was calibrated against the corneometer data $Cor(t)$ through linear regression. The calibration equation is given by

$$E_{\text{tcal}}(t) = \frac{K_1 \times (\text{Cor}(t) - d_1)}{K_2} + d_2 \quad (7)$$

where $K_1 = -0.472$, $K_2 = -0.363$, $d_1 = 126.1$, and $d_2 = 76.63$ were obtained by fitting $E_{\text{tcal}}(t)$ and $\text{Cor}(t)$.

Experiments on Human Subjects: All measurement on human subjects were conducted under approval from the Institutional Review Board of the University of Texas at Austin (protocol number: 2015-05-0024). Informed consent was obtained from all subjects involved in the study.

Supporting Information

Supporting Information is available from the Wiley Online Library or from the author.

Acknowledgements

The modeling and experimental work on stretchable antenna was supported by the US National Science Foundation (NSF) Division of Electrical, Communications and Cyber Systems (ECCS) under Grant No. 1509767. After the NSF grant ended, the antenna research was sponsored by the Army Research Laboratory (ARL) and was accomplished under Cooperative Agreement Number W911NF-19-2-0036. The biometric sensor development and human subject validation was supported by the US Office of Naval Research (ONR) under Grant No. N00014-16-1-2044.

The views and conclusions contained in this document are those of the authors and should not be interpreted as representing the official policies, either expressed or implied, of the National Science Foundation, Army Research Office nor the Office of Naval Research of the U.S. Government. The U.S. Government is authorized to reproduce and distribute reprints for the Government purposes notwithstanding any copyright notation herein. H.J. led the development of the concept, device design, and fabrication, as well as all of the measurements. L.W. led the mechanical FEM and X.Y. led the RF simulations. T.H. contributed to the programming for the pulse oximetry. H.J. led the fabrication, with supports from R.M. and Z.D. S.Q and K.H contributed to the ECG and pulse oximetry measurement. L.S. and N.S. provided circuit and RF measurement guidance. N.L. proposed and supervised the whole project. H.J., L.W., R.M., and N.L. wrote the paper.

Conflict of Interest

The authors declare no conflict of interest.

Keywords

cut-solder-paste, electronic tattoo, flexible electronics, modular, near-field communication (NFC), reconfigurable

Received: February 9, 2019

Revised: March 20, 2019

Published online:

- [1] a) M. L. Hammock, A. Chortos, B. C.-K. Tee, J. B.-H. Tok, Z. Bao, *Adv. Mater.* **2013**, *25*, 5997; b) T. Someya, T. Sekitani, S. Iba, Y. Kato, H. Kawaguchi, T. Sakurai, *Proc. Natl. Acad. Sci. USA* **2004**, *101*, 9966.
- [2] a) D.-H. Kim, N. Lu, R. Ma, Y.-S. Kim, R.-H. Kim, S. Wang, J. Wu, S. M. Won, H. Tao, A. Islam, K. J. Yu, T.-i. Kim, R. Chowdhury, M. Ying, L. Xu, M. Li, H.-J. Chung, H. Keum, M. McCormick, P. Liu,

- Y.-W. Zhang, F. G. Omenetto, Y. Huang, T. Coleman, J. A. Rogers, *Science* **2011**, *333*, 838; b) S. Kabiri Ameri, R. Ho, H. Jang, L. Tao, Y. Wang, L. Wang, D. M. Schnyer, D. Akinwande, N. Lu, *ACS Nano* **2017**, *11*, 7634.
- [3] J.-W. Jeong, W.-H. Yeo, A. Akhtar, J. J. S. Norton, Y.-J. Kwack, S. Li, S.-Y. Jung, Y. Su, W. Lee, J. Xia, H. Cheng, Y. Huang, W.-S. Choi, T. Bretl, J. A. Rogers, *Adv. Mater.* **2013**, *25*, 6839.
- [4] Y. Liu, J. J. S. Norton, R. Qazi, Z. Zou, K. R. Ammann, H. Liu, L. Yan, P. L. Tran, K.-I. Jang, J. W. Lee, D. Zhang, K. A. Kilian, S. H. Jung, T. Bretl, J. Xiao, M. J. Slepian, Y. Huang, J.-W. Jeong, J. A. Rogers, *Sci. Adv.* **2016**, *2*, e1601185.
- [5] R. C. Webb, A. P. Bonifas, A. Behnaz, Y. Zhang, K. J. Yu, H. Cheng, M. Shi, Z. Bian, Z. Liu, Y.-S. Kim, W.-H. Yeo, J. S. Park, J. Song, Y. Li, Y. Huang, A. M. Gorbach, J. A. Rogers, *Nat. Mater.* **2013**, *12*, 938.
- [6] X. Huang, H. Cheng, K. Chen, Y. Zhang, Y. Zhang, Y. Liu, C. Zhu, S.-c. Ouyang, G.-W. Kong, C. Yu, Y. Huang, J. A. Rogers, *IEEE Trans. Biomed. Eng.* **2013**, *60*, 2848.
- [7] C. Dagdeviren, Y. Shi, P. Joe, R. Ghaffari, G. Balooch, K. Usgaonkar, O. Gur, P. L. Tran, J. R. Crosby, M. Meyer, Y. W. Su, R. C. Webb, A. S. Tedesco, M. J. Slepian, Y. G. Huang, J. A. Rogers, *Nat. Mater.* **2015**, *14*, 728.
- [8] C. H. Wang, X. S. Li, H. J. Hu, L. Zhang, Z. L. Huang, M. Y. Lin, Z. R. Zhang, Z. N. Yin, B. Huang, H. Gong, S. Bhaskaran, Y. Gu, M. Makihata, Y. X. Guo, Y. S. Lei, Y. M. Chen, C. F. Wang, Y. Li, T. J. Zhang, Z. Y. Chen, A. P. Pisano, L. F. Zhang, Q. F. Zhou, S. Xu, *Nat. Biomed. Eng.* **2018**, *2*, 687.
- [9] a) J. Kim, G. A. Salvatore, H. Araki, A. M. Chiarelli, Z. Xie, A. Banks, X. Sheng, Y. Liu, J. W. Lee, K.-I. Jang, S. Y. Heo, K. Cho, H. Luo, B. Zimmerman, J. Kim, L. Yan, X. Feng, S. Xu, M. Fabiani, G. Gratton, U. Paik, J. A. Rogers, *Sci. Adv.* **2016**, *2*, e1600418; b) H. Li, Y. Xu, X. Li, Y. Chen, Y. Jiang, C. Zhang, B. Lu, J. Wang, Y. Ma, Y. Chen, *Adv. Healthcare Mater.* **2017**, *6*, 1601013; c) Y. Lee, H. Lee, J. Jang, J. Lee, M. Kim, J. Lee, H. Kim, K.-R. Lee, K. Kim, H. Cho, presented at *2016 IEEE International Solid-State Circuits Conference (ISSCC)*, San Francisco, CA, USA, February **2016**.
- [10] a) W. Gao, S. Emaminejad, H. Y. Y. Nyein, S. Challa, K. V. Chen, A. Peck, H. M. Fahad, H. Ota, H. Shiraki, D. Kiriya, D. H. Lien, G. A. Brooks, R. W. Davis, A. Javey, *Nature* **2016**, *529*, 509; b) Y. J. Hong, H. Lee, J. Kim, M. Lee, H. J. Choi, T. Hyeon, D. H. Kim, *Adv. Funct. Mater.* **2018**, *28*, 1805754.
- [11] a) J. Kim, A. Banks, Z. Xie, S. Y. Heo, P. Gutruf, J. W. Lee, S. Xu, K.-I. Jang, F. Liu, G. Brown, J. Choi, J. H. Kim, X. Feng, Y. Huang, U. Paik, J. A. Rogers, *Adv. Funct. Mater.* **2015**, *25*, 4761; b) J. Kim, P. Gutruf, A. M. Chiarelli, S. Y. Heo, K. Cho, Z. Xie, A. Banks, S. Han, K.-I. Jang, J. W. Lee, K.-T. Lee, X. Feng, Y. Huang, M. Fabiani, G. Gratton, U. Paik, J. A. Rogers, *Adv. Funct. Mater.* **2017**, *27*, 1604373; c) S. P. Lee, G. Ha, D. E. Wright, Y. J. Ma, E. Sen-Gupta, N. R. Haubrich, P. C. Branche, W. H. Li, G. L. Huppert, M. Johnson, H. B. Mutlu, K. Li, N. Sheth, J. A. Wright, Y. G. Huang, M. Mansour, J. A. Rogers, R. Ghaffari, *npj Digital Med.* **2018**, *1*, 2; d) S. R. Krishnan, C. J. Su, Z. Xie, M. Patel, S. R. Madhvapathy, Y. Xu, J. Freudman, B. Ng, S. Y. Heo, H. Wang, *Small* **2018**, *14*, 1803192.
- [12] a) P. M. Barrett, R. Komatireddy, S. Haaser, S. Topol, J. Sheard, J. Encinas, A. J. Fought, E. J. Topol, *Am. J. Med.* **2014**, *127*, 95.e11; b) S. Xu, Y. H. Zhang, L. Jia, K. E. Mathewson, K. I. Jang, J. Kim, H. R. Fu, X. Huang, P. Chava, R. H. Wang, S. Bhole, L. Z. Wang, Y. J. Na, Y. Guan, M. Flavin, Z. S. Han, Y. G. Huang, J. A. Rogers, *Science* **2014**, *344*, 70; c) Y. Khan, M. Garg, Q. Gui, M. Schadt, A. Gaikwad, D. G. Han, N. A. D. Yamamoto, P. Hart, R. Welte, W. Wilson, S. Czarnecki, M. Poliks, Z. P. Jin, K. Ghose, F. Egitto, J. Turner, A. C. Arias, *Adv. Funct. Mater.* **2016**, *26*, 8764; d) Z. L. Huang, Y. F. Hao, Y. Li, H. J. Hu, C. H. Wang, A. Nomoto, T. S. Pan, Y. Gu, Y. M. Chen, T. J. Zhang, W. X. Li, Y. S. Lei, N. Kim, C. F. Wang, L. Zhang, J. W. Ward, A. Maralani, X. S. Li, M. F. Durstock, A. Pisano, Y. Lin, S. Xu, *Nat. Electron.* **2018**, *1*, 473.

- [13] S. Yang, Y.-C. Chen, L. Nicolini, P. Pasupathy, J. Sacks, B. Su, R. Yang, D. Sanchez, Y.-F. Chang, P. Wang, D. Schnyer, D. Neikirk, N. Lu, *Adv. Mater.* **2015**, 27, 6423.
- [14] T. Widlund, S. X. Yang, Y. Y. Hsu, N. S. Lu, *Int. J. Solids Struct.* **2014**, 51, 4026.
- [15] J. W. Lee, R. X. Xu, S. Lee, K. I. Jang, Y. C. Yang, A. Banks, K. J. Yu, J. Kim, S. Xu, S. Y. Ma, S. W. Jang, P. Won, Y. H. Li, B. H. Kim, J. Y. Choe, S. Huh, Y. H. Kwon, Y. G. Huang, U. Paik, J. A. Rogers, *Proc. Natl. Acad. Sci. USA* **2016**, 113, 6131.
- [16] S. X. Yang, S. T. Qiao, N. S. Lu, *J Appl Mech-T Asme* **2017**, 84.
- [17] K.-I. Jang, K. Li, H. U. Chung, S. Xu, H. N. Jung, Y. Yang, J. W. Kwak, H. H. Jung, J. Song, C. Yang, *Nat. Commun.* **2017**, 8, 15894.
- [18] a) X. Huang, H. Cheng, K. Chen, Y. Zhang, Y. Zhang, Y. Liu, C. Zhu, S.-c. Ouyang, G.-W. Kong, C. Yu, *IEEE Trans. Biomed. Eng.* **2013**, 60, 2848; b) X. Huang, Y. H. Liu, H. Y. Cheng, W. J. Shin, J. A. Fan, Z. J. Liu, C. J. Lu, G. W. Kong, K. Chen, D. Patnaik, S. H. Lee, S. Hage-Ali, Y. G. Huang, J. A. Rogers, *Adv. Funct. Mater.* **2014**, 24, 3846.
- [19] S. Krishnan, Y. Z. Shi, R. C. Webb, Y. J. Ma, P. Bastien, K. E. Crawford, A. Wang, X. Feng, M. Manco, J. Kurniawan, E. Tir, Y. G. Huang, G. Balooch, R. M. Pielak, J. A. Rogers, *Microsyst. Nanoeng.* **2017**, 3, 17014.
- [20] Y. Wang, Y. Qiu, S. K. Ameri, H. Jang, Z. Dai, Y. Huang, N. Lu, *npj Flexible Electron.* **2018**, 2, 6.
- [21] R. Rangarajan, J. Von Arx, K. Najafi, presented at *43rd IEEE Midwest Symposium on Circuits and Systems*, Lansing, MI August **2000**.
- [22] T. J. Harpster, B. Stark, K. Najafi, *Sens. Actuators, A* **2002**, 95, 100.
- [23] a) J. Kim, A. Banks, H. Y. Cheng, Z. Q. Xie, S. Xu, K. I. Jang, J. W. Lee, Z. J. Liu, P. Gutruf, X. Huang, P. H. Wei, F. Liu, K. Li, M. Dalal, R. Ghaffari, X. Feng, Y. G. Huang, S. Gupta, U. Paik, J. A. Rogers, *Small* **2015**, 11, 906; b) Z. H. Jiang, D. E. Brocker, P. E. Sieber, D. H. Werner, *IEEE Trans. Antennas Propag.* **2014**, 62, 4021.
- [24] C. M. Lochner, Y. Khan, A. Pierre, A. C. Arias, *Nat. Commun.* **2014**, 5, 5745.
- [25] R. Ortega, C. J. Hansen, K. Elterman, A. Woo, *N. Engl. J. Med.* **2011**, 364, e33.
- [26] a) W. Zijlstra, A. Buursma, W. Meeuwse-Van der Roest, *Clin. Chem.* **1991**, 37, 1633; b) F. Fabbri, A. Sassaroli, M. E. Henry, S. Fantini, *Phys. Med. Biol.* **2004**, 49, 1183.

**ADVANCED
MATERIALS
TECHNOLOGIES**

Supporting Information

for *Adv. Mater. Technol.*, DOI: 10.1002/admt.201900117

**Modular and Reconfigurable Wireless E-Tattoos for
Personalized Sensing**

*Hyoyoung Jeong, Liu Wang, Taewoo Ha, Ruchika Mitbander,
Xiangxing Yang, Zhaohe Dai, Shutao Qiao, Linxiao Shen, Nan
Sun, and Nanshu Lu**

Supporting Information

Modular and Reconfigurable Wireless E-Tattoos for Personalized Sensing

*Hyoyoung Jeong, Liu Wang, Taewoo Ha, Ruchika Mitbander, Xiangxing Yang, Zhaohe Dai, Shutao Qiao, Linxiao Shen, Nan Sun, Nanshu Lu**

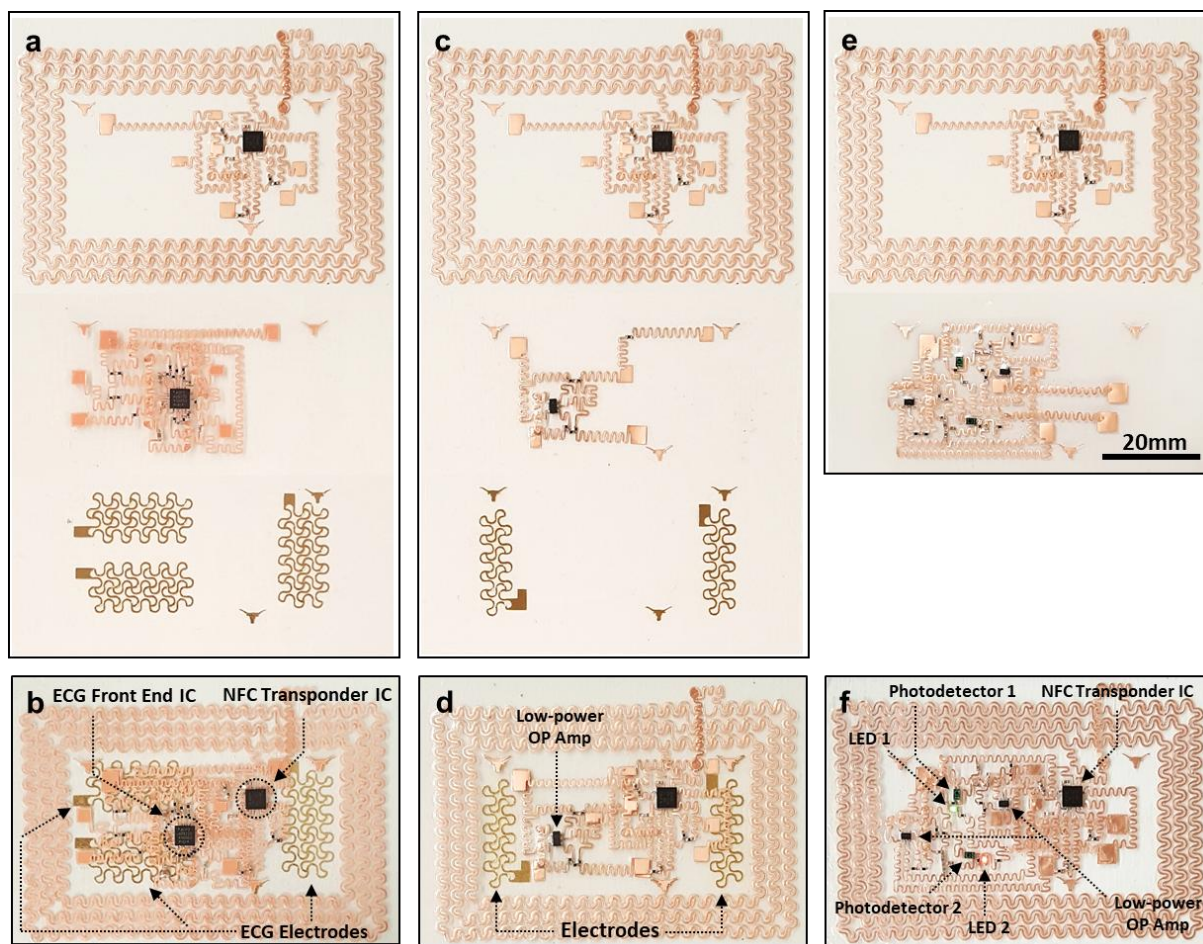


Figure S2. Photos of the individual e-tattoo layers and assembled multilayer e-tattoos. a) Individual layers of an NFC-enabled ECG tattoo, from top down: NFC layer, ECG circuit layer, and electrode layer. b) The assembled ECG e-tattoo. c) Individual layers of an NFC-enabled skin hydration tattoo, from top down: NFC layer, skin hydration circuit layer, and electrode layer. d) The assembled skin hydration e-tattoo. e) Individual layers of an NFC-enabled SpO₂ tattoo, from top down: NFC layer, SpO₂ circuit layer. f) The assembled SpO₂ e-tattoo.

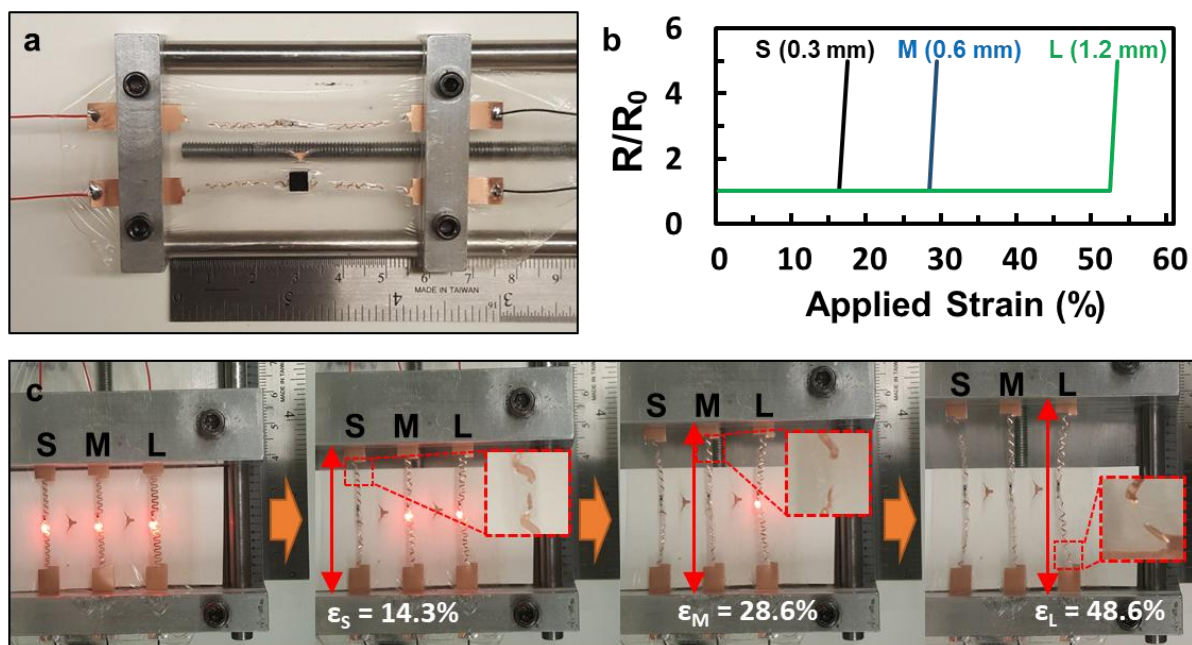


Figure S3. Optimization of serpentine design. a) Red LED and NFC IC soldered with serpentine-shaped stretchable Cu interconnects stretched to the rupturing point. b) End-to-end resistance as a function of applied strain with three different arm lengths in the serpentine design: 0.3 mm (“S”), 0.6 mm (“M”), and 1.2 mm (“L”), and the strain-to-rupture was measured to be 16.5%, 28.5%, and 52.5%, respectively. c) Photos of the three types of serpentine under deformation. The insets highlight the ruptured regions, which are always away from the rigid LED.

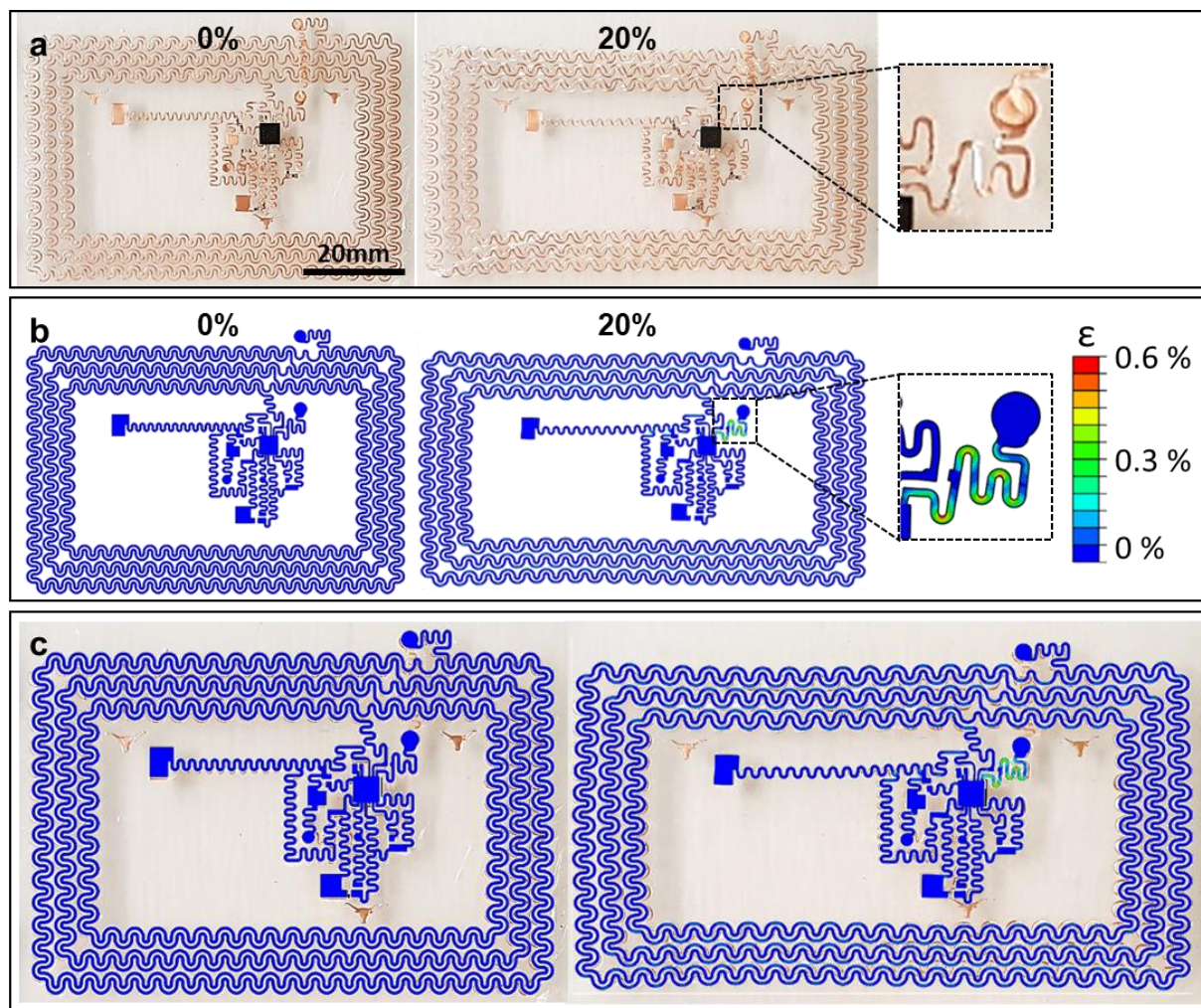


Figure S4. Comparison of the experimental and FEM results of a single layer e-tattoo under 0 and 20% uniaxial strain. a) Experimental photos of an undeformed and 20% stretched e-tattoo. The inset highlights the most deformed region of the circuit. b) Corresponding FEM contour plots of the maximum principle strains. c) Experimental and FEM images fully overlapped for undeformed and deformed e-tattoo.

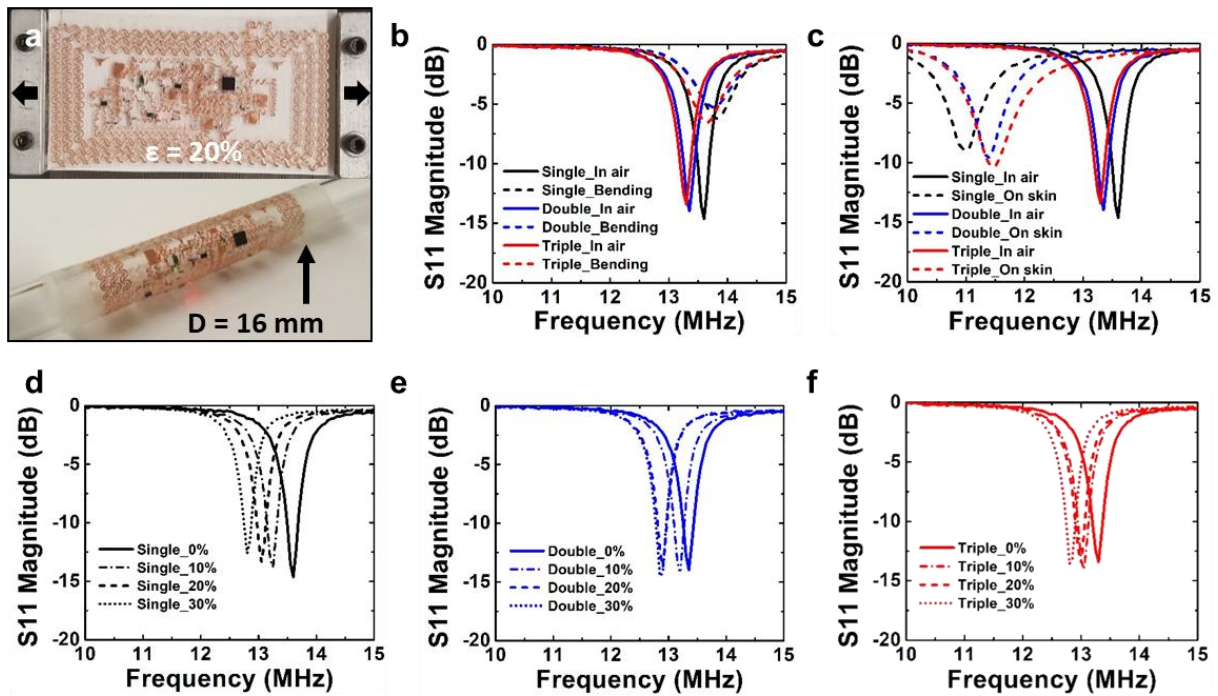


Figure S5. Electromagnetic-mechanical characteristics of e-tattoos. a) E-tattoos with lighting green LED subjected to stretching and bending. b) The measured S11 magnitude of the reflected signal for e-tattoos under bending: single layer (NFC), double layer (NFC+ECG), and triple layer (NFC+ECG+electrodes). c) Body loading effects in the air and on the skin. d-f) Tensile strain effects for (d) single (e) double and (f) triple layer e-tattoos.

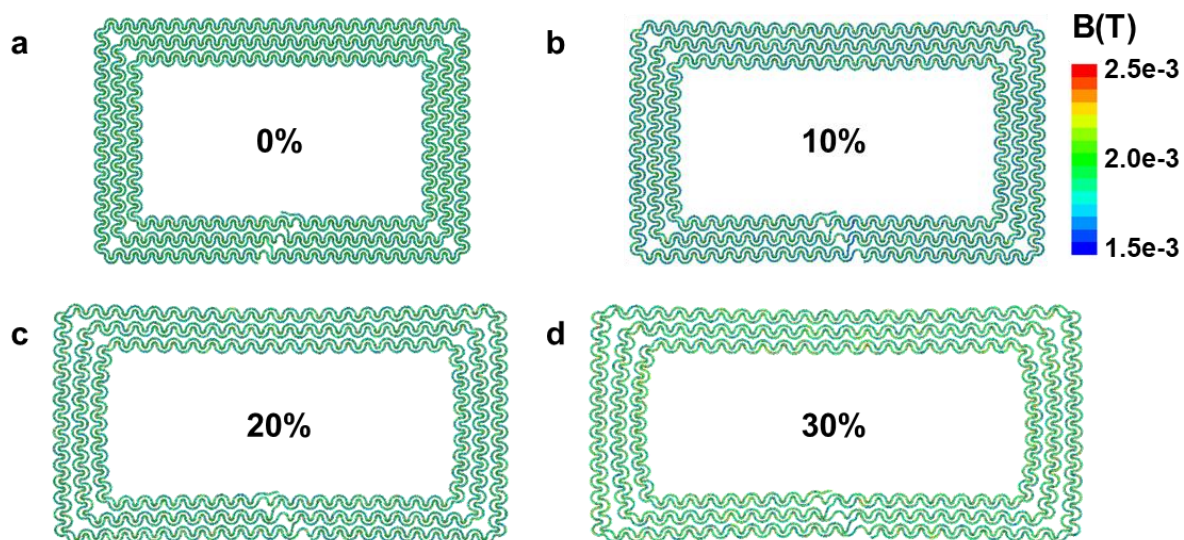


Figure S6. ANSYS Maxwell FEM results of the magnetic flux density field (B field) after stretching the PSA by (a) 0%, (b) 10%, (c) 20%, and (d) 30%.

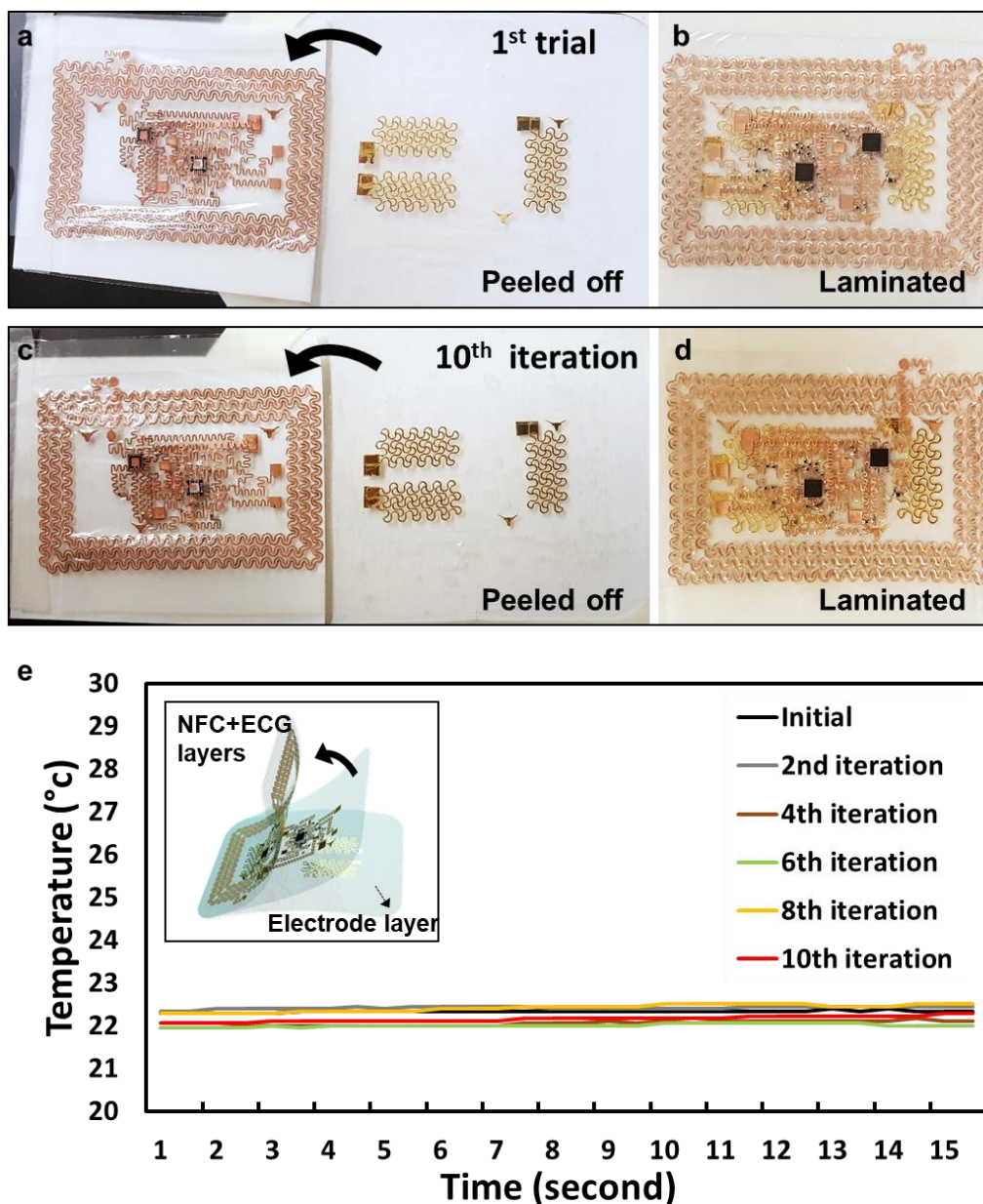


Figure S7. Repeated assembly and disassembly of the triple layer ECG e-tattoo. a) Disassembly by peeling off the NFC+ECG layer from the electrode layer. b) Image of the laminated ECG e-tattoo after one time of disassembly and reassembly. c) Peeling off the NFC+ECG layer from the electrode layer after 10th iteration. d) Image of the assembled ECG e-tattoo after 10 times of disassembly and reassembly. e) Wirelessly measured ambient temperature after 1st, 2nd, 4th, 6th, 8th, and 10th assembly. Inset is a schematic of the ECG e-tattoo.

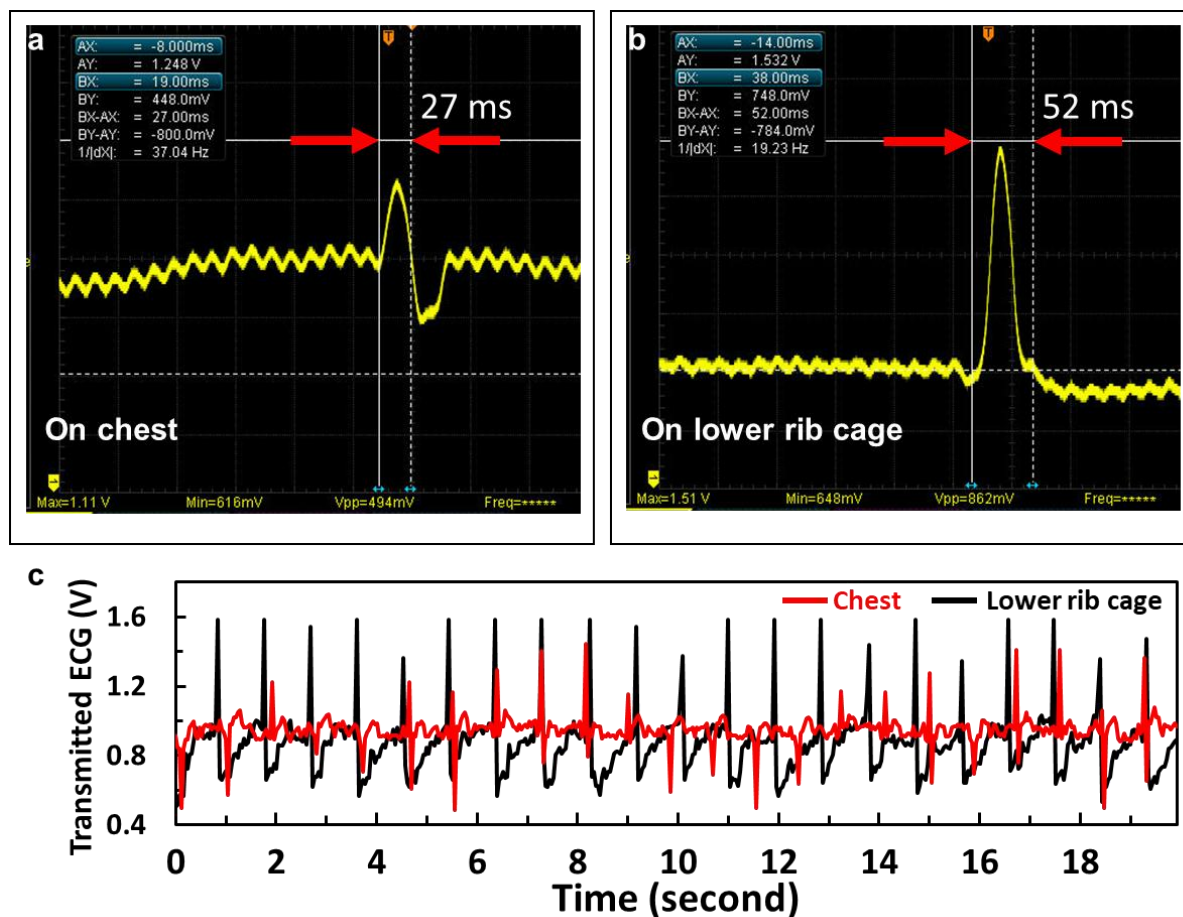


Figure S8. ECG signals measured at different lead placements. a) ECG measured on the chest. b) ECG measured from the lower left rib cage. c) Wirelessly transmitted ECG data from the e-tattoo mounted on the chest (red) and on the lower rib cage (black).

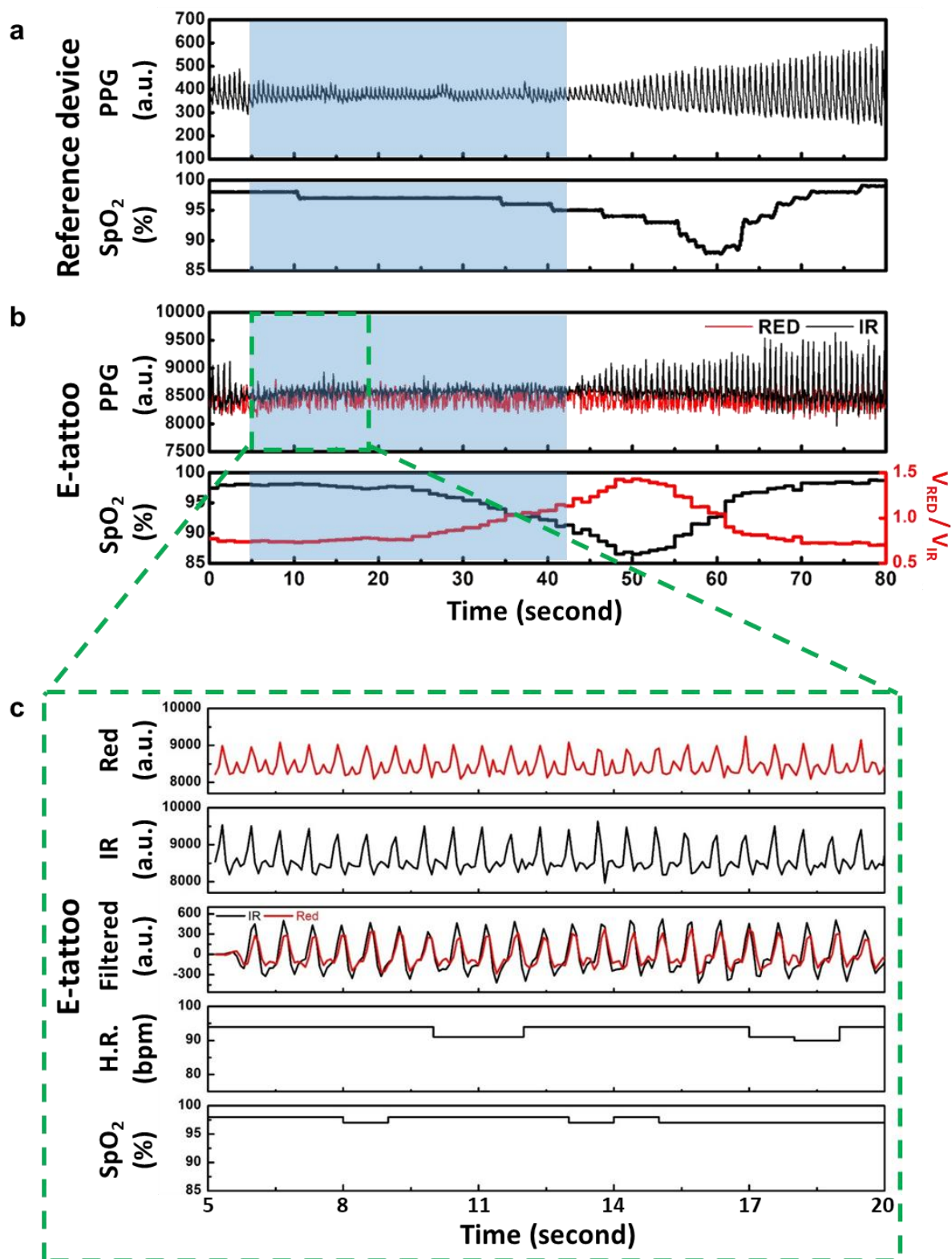


Figure S9. Pulse oximetry monitoring. Dynamic PPG and SpO₂ measured by a) a commercial oximeter and b) a SpO₂ e-tattoo. The blue shaded regions label the breath holding phase. c) Blown-up view between 5 s – 20 s, from top down: the raw data from the red and IR LEDs, the filtered data, and the calculated HR and SpO₂.

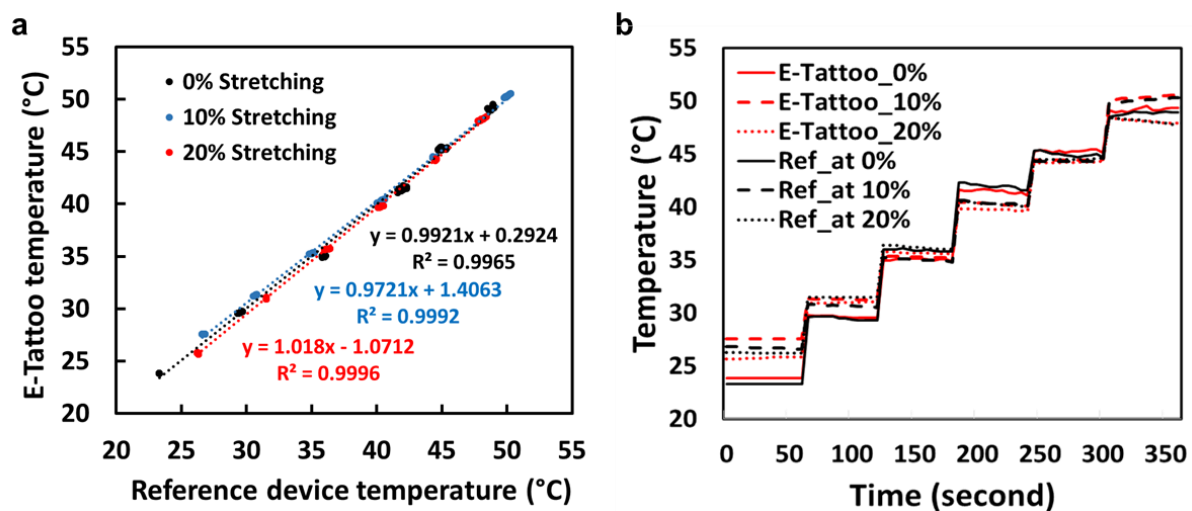
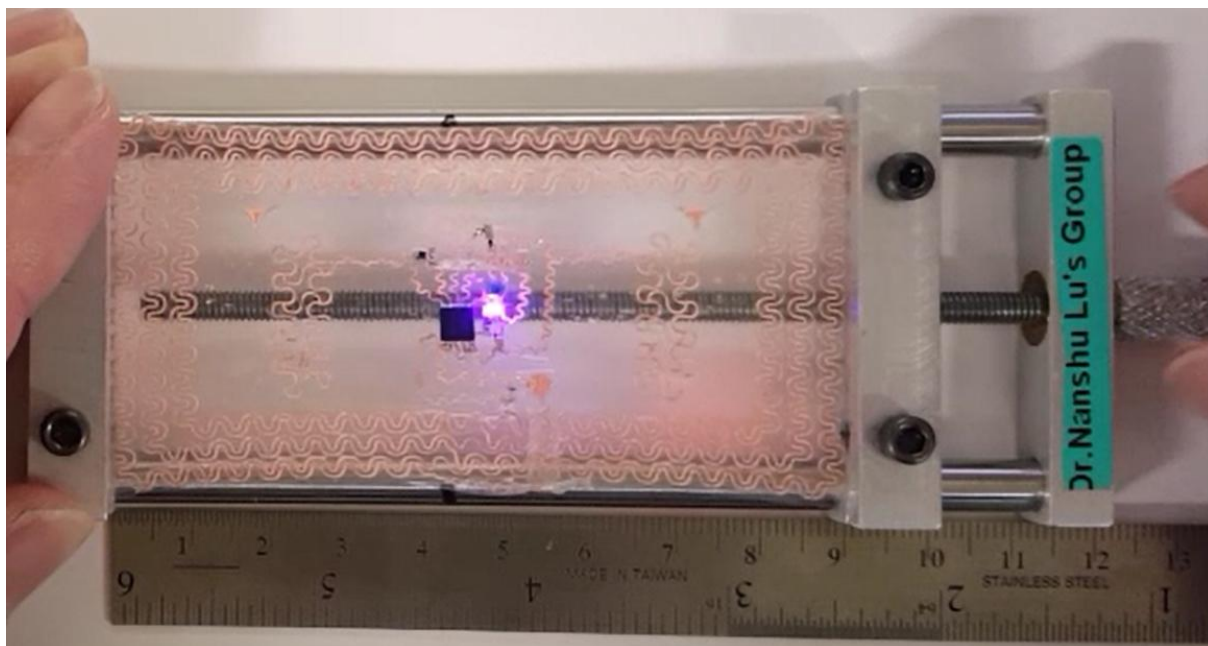


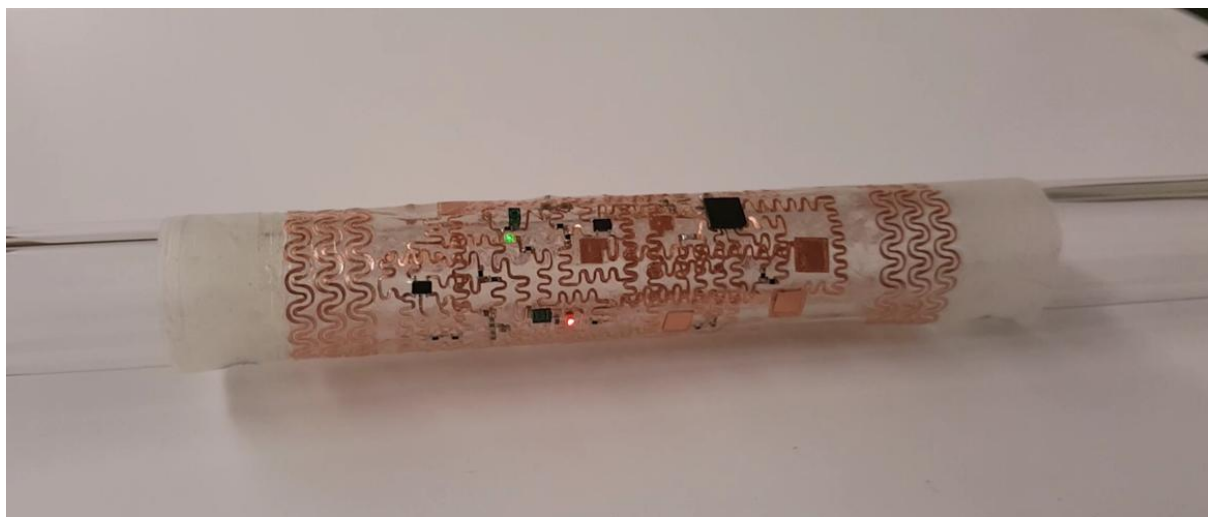
Figure S10. Validation of temperature e-tattoo. a) E-tattoo measured temperature plotted against temperature measured by a commercial thermocouple on the same hotplate when different strains were applied to the e-tattoo: 0% (black), 10% (blue), and 20% (red). b) Both types of data are plotted against time to show time stability of temperature e-tattoo.



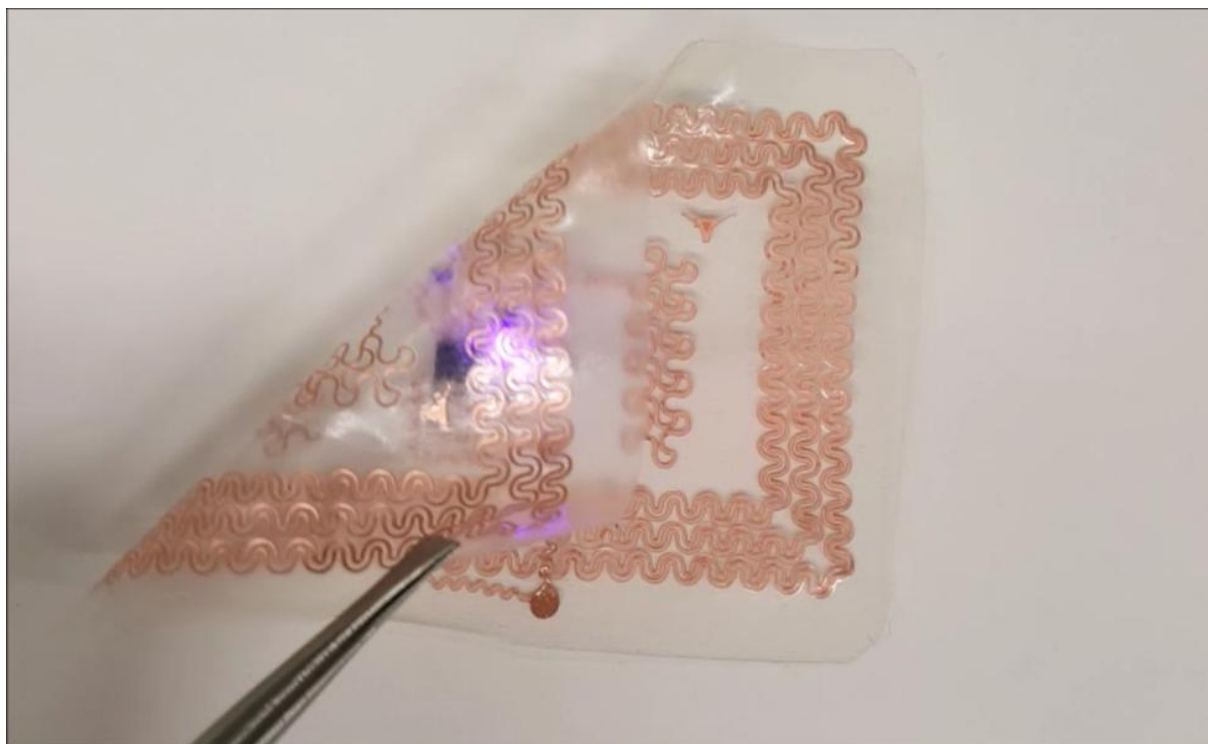
Movie S1. Wireless power transmission between NFC interrogator and e-tattoo under water flow. The LED was wirelessly turned on by the NFC interrogator while the e-tattoo attached on the skin was subjected to flowing water, demonstrating the water resistance of the e-tattoo.



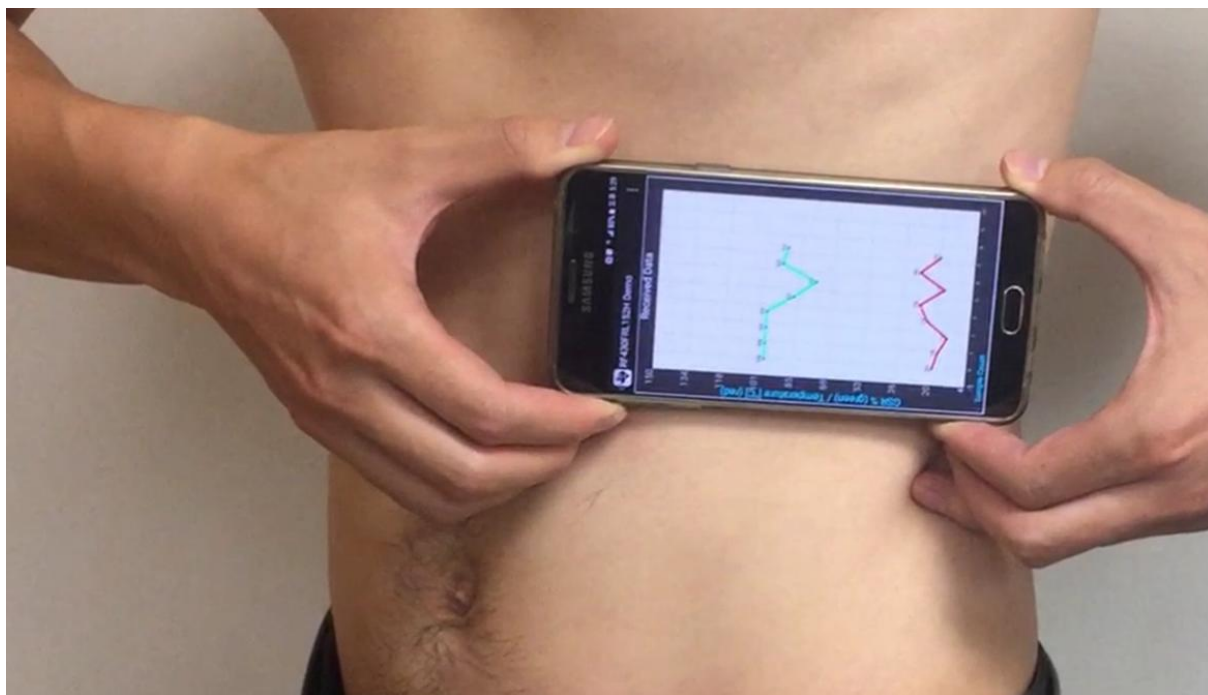
Movie S2. E-tattoo operation under stretching. The e-tattoo was stretched up to 20% with the LED wirelessly turned on by an NFC interrogator concealed beneath the white paper. (2x speed)



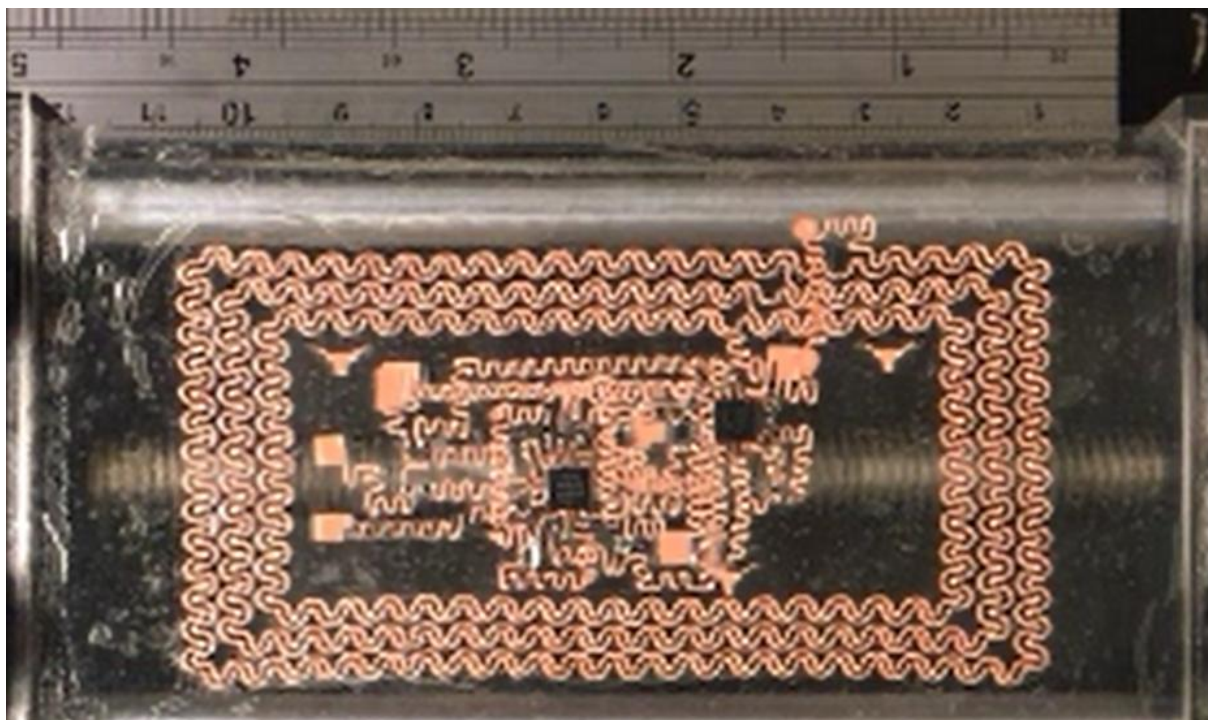
Movie S3. The SpO₂ e-tattoo operation under bending. The SpO₂ e-tattoo was wrapped on a 1.6 cm diameter tube with the two LEDs wirelessly turned on by an NFC interrogator underneath the white paper.



Movie S4. E-tattoo operation under folding. The LED was wirelessly turned on by the NFC interrogator underneath the white paper. (2x speed)



Movie S5. Power and data transmission between the SpO₂ e-tattoo on the skin and the smartphone. The green and red curves indicate the reflected ambient light signals.



Movie S6. The ECG e-tattoo operation under stretching. The e-tattoo was stretched up to 20% while the smart-phone was still able to read from the tattoo: the green curve indicates the ECG signal (no signal as not attached on the body), and the red curve indicates the ambient temperature. (2x speed)